ELSEVIER

Quaternary Science Reviews 23 (2004) 359–388

QSR

A geophysically constrained large ensemble analysis of the deglacial history of the North American ice-sheet complex

L. Tarasov, W. Richard Peltier*

Department of Physics, University of Toronto, Toronto, Ont., Canada M5S 1A7

Received 14 May 2003; accepted 7 August 2003

Abstract

Past reconstructions of the deglaciation history of the North American (NA) ice-sheet complex have relied either on largely unconstrained and limited explorations of the phase space of solutions produced by glaciological models or upon geophysical inversions of relative sea-level (RSL) data which suffer from incomplete geographic coverage of the glaciated regions, load history amplitude/timing ambiguities, and a lack of a priori glaciological self-consistency. As a first step in the development of a much more highly constrained deglaciation history, we present a synthesis of these two previously disjoint methodologies based on a large ensemble of glacial cycle simulations using a three-dimensional thermo-mechanically coupled ice-sheet model. Twenty glacial system model parameters, chosen so as to best cover the true deglacial phase space, were varied across the ensemble. Furthermore, a new high-resolution digitized ice margin chronology was imposed on the model in order to significantly limit the uncertainties associated with deglacial climate forcing. The model is simultaneously constrained by a large set of high-quality RSL histories, a space geodetic observation of the present-day rate of vertical motion of the crust from Yellowknife and a traverse of absolute gravity measurements from the west coast of Hudson Bay southward into Iowa.

The general form of the Last Glacial Maximum (LGM) ice topography that ensues when model results are subject to geophysical constraints is an ice sheet dominated by a large (3.3–4.3 km maximum ice thickness) Keewatin dome to the west of Hudson Bay connected to a major ice ridge running southeast to the Great Lakes, together with a Hudson Bay region that has relatively thin ice and an Arctic region heavily incised by open water and/or ice shelves. Geographically restricted fast flows due to sub-glacial till deformation are shown to be critical to obtaining such a multi-domed late glacial Laurentide Ice Sheet structure, one that has been previously inferred on the basis of geomorphological data and that is required to fit the geophysical constraints. Our results further suggest that the NA contribution to LGM eustatic sea-level drop is likely to be in the range of 60–75 m.

1. Introduction

The deglaciation history of the North American (NA) ice-sheet complex has been inferred on the basis of geophysical constraints alone (Peltier, 1994) in conjunction with geological inferences of ice extent (Dyke and Prest, 1987). However, such reconstructions have ice thickness that is unconstrained in regions from which the required geophysical data are unavailable and furthermore lack any constraint that might ensure them to be glaciologically self-consistent. Geophysical reconstructions also suffer from the ambiguity between load magnitude and the timing of load removal. An increase in surface mass load, for instance, can be accommodated by earlier ice load removal. On the other hand, dynamical ice-sheet models (ISMs) produce physically self-consistent ice sheets which thus further constrain load profiles and the history of load variation, but suffer due to their high sensitivity to the poorly constrained climate forcing as well as from uncertainties associated with basal processes and ice calving. Dynamical ISMs also allow further contact with glaciological observations concerning, for instance, the presence of fast ice flow and temperate ice (based on associated landforms, e.g. Kleman and Hattestrand, 1999; Stokes and Clark, 2001), and flow directions (inferred from striation patterns in bedrock and erratic dispersal patterns, e.g. Dyke et al., 2002).

It is clear that an amalgamation of these two approaches would be expected to lead to a much more highly constrained reconstruction of deglacial history.

*Corresponding author. Tel.: +1-416-978-2938; fax: +1-416-978-8905.

E-mail addresses: lev@atmosp.physics.utoronto.ca (L. Tarasov), peltier@atmosp.physics.utoronto.ca (W.R. Peltier).

0277-3791/$ - see front matter © 2003 Elsevier Ltd. All rights reserved.
doi:10.1016/j.quascirev.2003.08.004

Such a synthesis of methodologies has already been introduced in the context of efforts to reconstruct the evolution of the Greenland Ice Sheet (Tarasov and Peltier, 2002, 2003). The application of geophysical constraints to dynamical models of NA ice-sheet evolution represents a much more formidable challenge due to the large number of geophysical and geomorphological observations that are available, to the convoluted nature of Arctic shorelines where poorly constrained calving dynamics may have had critical impacts, and to the absence of a well-constrained model of climate forcing for such a geographically immense region. Past dynamical modelling studies of the NA ice complex have employed either intermediate complexity climate models (e.g. Deblonde et al., 1992; Tarasov and Peltier, 1997, 1999) or have used glacial indices derived from the Greenland Summit (GRIP) $\delta^{18}O$ chronology to interpolate between present-day observed and Last Glacial Maximum (LGM) climate fields obtained from a single General Circulation Model (GCM) snapshot reconstruction of the LGM climate state (e.g. Marshall et al., 2000, 2002). Results from the Paleoclimate Model Intercomparison Project (PMIP), however, indicate significant differences in climate fields predicted by the current generation of GCMs (Pollard and PMIP-participating groups, 2000). This fact, together with the large uncertainty arising from the application of a single down-wind paleoclimate proxy to fix the time evolution of climate fields, suggests that a much more complete accounting for the influence of climate uncertainty is required.

Previously developed dynamical models of the evolution of the Laurentide Ice Sheet (e.g. Tarasov and Peltier, 1999; Marshall et al., 2000) have generally delivered Laurentide Ice Sheet topographies at LGM characterized by a single dome (centered over or in close proximity to Hudson Bay) in contradistinction to both glaciological inferences (Dyke and Prest , 1987) and to the results of recent geophysical analyses (Peltier, 2002a) based upon the interpretation of new geodetic and absolute gravity measurements from Western Canada. Whether this disagreement between the results of these two methodologies is due to limitations in the representation of the ice dynamics, problems with the climate forcing, or a problem with the geophysically inferred LGM ice topography, clearly deserves attention. It is even unclear on a priori grounds whether current dynamical models are reconcilable with the existing broad set of geophysical constraints without imposing implausible ad hoc model forcings.

In this paper, we will therefore examine the impact of relative sea level (RSL) and other geophysical constraints on the deglaciation history of the NA ice-sheet complex predicted by a state-of-the-art thermomechanically coupled three-dimensional (3D) ISM. Furthermore, we will base our analyses on a large ensemble of model runs that incorporates 16 ensemble parameters to account for climate forcing uncertainty along with four parameters to account for uncertainties with respect to ice calving and till deformation. The incorporation of a newly available high-resolution ice margin chronology will be shown to significantly limit the impact of climate forcing uncertainty and thereby lead to the construction of a much more robust model of ice-sheet evolution, one that not only largely satisfies the geophysical constraints but is also glaciological plausible. In the next section of this paper, a description of the model components is provided. Subsequent sections examine ensemble results, best model fits, and some remaining model uncertainties. Conclusions, together with a discussion of remaining issues, are provided in the final section of the paper.

2. Discussion of model components

The University of Toronto Glacial Systems Model consists of six interacting sub-components representing, respectively, thermomechanically coupled ice-sheet dynamics, basal dynamics, surface mass balance, ice calving, bedrock deflection due to changes in surface loading, and climate forcing. Many of these components suffer from a lack of robustness due to dependence upon poorly constrained parameters. A primary challenge in this work has therefore been to identify a computationally tractable set of ensemble parameters that can encompass much of the uncertainty embodied in the glacial system model. After an extensive search involving thousands of model runs and neural network-based parameter relevancy analyses (Bishop, 1995; Goodman and Harrel, 1999), we have settled on a set of 20 parameters that are varied through extremal ranges in order to construct the ensemble of model runs to be discussed herein. These parameters are listed in Table 1 and are discussed in the following subsections. Additional constant model parameters are summarized in Table 2.

2.1. Core ISM

As the ISM has been fully described elsewhere (Tarasov and Peltier, 1999, 2002), only a brief description is presented herein. The 3D thermomechanically coupled ISM uses the standard Glen flow law for the ice rheology to compute the horizontal ice velocity $\mathbf{V}(\mathbf{r})$ as

$$\mathbf{V}(\mathbf{r}) = \mathbf{V}_b - 2(\rho_i g)^n \{\nabla_h(h)\cdot\nabla_h(h)\}^{(n-1)/2}\nabla_h(h) \times E\int_{z_b}^{z} A(T^*(z'))(h-z')^n\,dz' \quad (1)$$

Table 1
Ensemble parameters

Definition	Parameter	Range
Till viscosity	μ_0	$2.5\times10^{9}\rightarrow1\times10^{11}$ Pa s
Maximum calving velocity	U_{Cmx}	$0.4\rightarrow2.6$ km yr^{-1}
High-temperature calving cutin	T_{Chi}	$-18\rightarrow0^{\circ}$C
Regional northwestern maximum calving velocity	U_{CNWmx}	$0.2\rightarrow1.8$ km yr^{-1}
Global LGM precipitation scale factor	fP	$0.8\rightarrow1.8$
Western Canada precipitation factor	$\mathrm{fP_W}$	$1.0\rightarrow3.5$
South-central precipitation enhancement factor	$\mathrm{RP_{SM}}$	$1.8\rightarrow3.4$
Precipitation phase factor	Θ_{P}	$0.4\rightarrow1.6$
Pre -30 kyr desert-elevation cutoff	des0	$0.7\rightarrow2.1$ km
Post -30 kyr western desert-elevation cutoff	desW	$2.5\rightarrow4.5$ km
Post -30 kyr northwestern desert-elevation cutoff	desNW	$0.\rightarrow2.$ km
Post -30 kyr north-central desert-elevation cutoff	desNC	$0.\rightarrow2.$ km
Post -30 kyr central desert-elevation cutoff	desC	$0.\rightarrow2.2$ km
Post -30 kyr remainder desert-elevation cutoff	des2	$1.4\rightarrow2.4$ km
Two LGM precipitation–evaporation EOF components	fPEOF[2]	150% of PMIP range
Global LGM temperature scale factor	fnT	$0.8\rightarrow1.3$
Three LGM temperature EOF components	fTEOF[3]	150% of PMIP range

Table 2
Model parameters

Definition	Parameter	Value
Earth radius	r_{e}	6370 km
Earth mass	m_{e}	5.976×10^{24} kg
Lithospheric thickness	L_{e}	100 km
Latent heat of fusion	L	3.35×10^{5} J kg^{-1}
Ice density	ρ_{i}	910 kg m^{-3}
Ice specific heat capacity	$c_{\mathrm{i}}(T)$	$(152.5+7.122T)$ J kg^{-1} K^{-1}
Ice thermal conductivity	$k_{\mathrm{i}}(T)$	$9.828\exp(-0.0057T)$ W m^{-1} K^{-1}
Bedrock density	ρ_{b}	3300 kg m^{-3}
Bedrock specific heat capacity	c_{b}	1000 J kg$^{-1}\circ$C^{-1}
Bedrock thermal conductivity	k_{b}	3 W m$^{-1}\circ$C^{-1}
Standard deviation, positive degree-day PDD model	σ	5.2°C
Standard deviation, accumulation model	σ_p	$\sigma-1^{\circ}$C
Number of ice thermodynamic levels	nz_{i}	65
Number of bed thermodynamic levels	nz_{b}	5
Longitudinal ISM grid resolution	$\Delta\phi$	1.0°
Latitudinal ISM grid resolution	$\Delta\theta$	0.5°
Weertman sliding law rate factor	k_{s}	$2.\times10^{-13}$ Pa^{-3} m^{2} yr^{-1}
Glen flow law constant, $T<-10^{\circ}$C	B_{gc}	1.14×10^{-5} Pa^{3} yr^{-1}
Glen flow law constant, $T>-10^{\circ}$C	B_{gw}	5.47×10^{10} Pa^{3} yr^{-1}
Flow law enhancement factor	E	6.5
Creep activation energy of ice, $T<-10^{\circ}$C	Q_{c}	6×10^{4} J mol^{-1}
Creep activation energy of ice, $T>-10^{\circ}$C	Q_{c}	1.39×10^{5} J mol^{-1}
Glen flow law exponent	n	3

with European Ice Sheet Model Intercomparison (EISMINT) project values for the temperature-dependent flow coefficient ($A(T)$) (Payne et al., 2000). Here subscript b refers to the bedrock surface, h is the ice surface elevation above sea level, ρ_{i} is the density of ice, g is the acceleration due to gravity, and n is the flow law exponent ($=3$). A flow enhancement parameter, E, of magnitude 6.5 has been selected in approximate accord with values for our best-fit dynamical models of the Greenland ice sheet at the same model resolution. Increasing this to a higher value of 10 has little impact on fits to RSL data and predicted ice volume, while values much higher than this are hard to justify on a priori grounds. The evolution of ice thickness (H) is computed using the vertically integrated form of the equation for the conservation of mass as

$$\frac{\partial H(x)}{\partial t}=-\nabla_{\mathrm{h}}\int_{z_{\mathrm{b}}}^{h}\mathbf{V}(\mathbf{r})\,\mathrm{d}z+G(\mathbf{r},T(\mathbf{r})), \tag{2}$$

in which G is the net surface and basal mass balance.

The computation of the ice temperature field (T) takes into account advection, vertical diffusion, and heat

generated by deformation heating (Q_d) as

$$\rho_i c_i(T(\mathbf{r}))\frac{\partial T(\mathbf{r})}{\partial t} = \frac{\partial}{\partial z}\left\{k_i(T(\mathbf{r}))\frac{dT(\mathbf{r})}{dz}\right\} - \rho_i c_i(T(\mathbf{r}))\mathbf{V}(\mathbf{r})\cdot \nabla T(\mathbf{r}) + Q_d(\mathbf{r}). \quad (3)$$

Boundary conditions account for heating due to sliding (Tarasov and Peltier, 1999). A one-dimensional (1D) (vertical diffusion only) bed-thermal model that spans a depth of 2 km is also incorporated for each grid point. The deep geothermal heat flux is taken to be that provided by the digital map of Pollack et al. (1993) with an ad hoc 10 mW/m^{-2} additional heat flux for Hudson Bay and the Gulf of Boothia to promote fast flow in these regions in order to better fit the observations.

2.2. Mass-balance model

The surface ablation model is based upon a Positive Degree-Day (PDD) method with temperature-dependent coefficients derived from energy balance calculations (Braithwaite, 1995) as described in Tarasov and Peltier (2002). The influence of surface refreezing is included by accounting for both capillary retention and latent heating following Janssens and Huybrechts (2000). Snow fractions are also computed using a normal statistical model to determine the monthly fraction of hourly temperatures below 2°C. Uncertainties in surface mass-balance parameters are absorbed by climate forcing uncertainties and as such no parameters associated with this component are varied in constructing the ensemble. As in previous model-based analyses (Tarasov and Peltier, 1999), we will continue to enforce ice-free conditions over Alaska in accord with the paleo record (Hamilton, 1994) by setting ablation to be no less than accumulation in this region.

The calving model is newly developed and is designed to account for both buoyancy effects as well as the blockage of drainage channels. Calving is assumed to require either greater than 600 m present-day bathymetry or all of the following conditions: (1) sea-surface mean summer temperature (T_s) above a critical minimum value (T_{Cmn}), (2) grid-box ice thickness less than 1.1 times the maximum buoyant thickness (H_{flot}), (3) an adjacent ice-free grid box with contemporaneous depth greater than 30 m, and (4) a corresponding regional drainage outlet that is ice free. These conditions attempt to capture the influence of sea-ice blockage of drainage channels as well as to incorporate current buoyancy control theories of calving for temperate tide-water glaciers (Vieli et al., 2001; Van der Veen, 2002). When the above conditions are met, the calving velocity is computed as

$$U_c = U_{Cmx} n_{edge} \min\left\{1, \left(\frac{1.1H_{flot} - H}{0.25H_{flot}}\right)^2\right\} \times \left(\exp\left(\frac{T_s - T_{Cmx}}{T_{Cmx} - T_{Cmn}}\right) - \exp(-1)\right) \Big/ \times (1 - \exp(-1)). \quad (4)$$

The model factors in the number of grid-box edges (n_{edge}) meeting the calving conditions and uses both the high-temperature set point (T_{Cmx}) and maximum calving velocity (U_{Cmx}) as ensemble parameters. Based on best fits from previous ensembles, T_{Cmn} is set to 5°C below T_{Cmx}. Sea level for the ISM (but not the RSL calculation) is forced on the basis of the SPECMAP $\delta^{18}O$ data set (Imbrie et al., 1984), assuming an LGM eustatic sea-level drop of 130 m. Our intention is to relax this assumption in future analyses.

2.3. Basal dynamics

When the base of an ice sheet approaches the pressure melting point, enhanced ice-sheet motion can occur due to basal sliding or deformation of sub-basal sediment. Although a strong case has been made for the critical influence of till deformation under certain sectors of the Laurentide ice sheet (Alley, 1991; Clark et al., 1996b; Licciardi et al., 1998), the role of till deformation in glacial dynamics continues to be actively debated (e.g. Piotrowski et al., 2002). To avoid a priori assumptions concerning till deformation, the viscosity of the till layer is taken to be an ensemble parameter (i.e. to be varied over the ensemble of runs). The following expression for the basal velocity ($U(z_b)$) of ice over deforming till is obtained on the basis of the following assumptions and approximations: (1) the effective pressure vanishes at the ice–till interface, (2) the shear stress of the till surface is equal to that of the basal ice, (3) the till layer is unfrozen whenever the basal ice is at the pressure melting point, (4) the till thickness is large enough so that the shear stress reaches the yield stress of the till, and (5) the till is Coulomb plastic

$$U(z_b) = f_b(x,y)\frac{1}{n+1}\tau^{n+1}\frac{\mu_0^{-n}}{(\rho_t - \rho_w)g\tan\phi}(2D_0)^{1-n}. \quad (5)$$

The till-deformation parameters consisting of the till-deformation exponent ($n = 1.25$), the sediment angle of internal friction ($\phi = 22°$), the density of till ($\rho_t = 2390\ kg/m^{-3}$), and the Newtonian reference deformation rate ($D_0 = 7.9^{-7}\ s^{-1}$), are taken from Jenson et al. (1996). Till viscosity (μ_0) is allowed to vary from a lower bound constrained by the model time step (2.5×10^9 Pa s) to an upper bound of 1×10^{11} Pa s. Preliminary analyses explored even higher values of the upper bound, but we have found that observational constraints favor lower viscosities as will be discussed in a

subsequent section. For comparison, observationally based estimates of effective till viscosity range from about 1×10^8 to 5×10^{11} Pa s (Paterson, 1994). Allowance of lower viscosities for the ensemble runs could allow stronger topographic variations on the ice surface and stronger temporal variation (thermocycling) of ice-stream activity. However, the higher ice velocities that would then ensue would make explicit accounting for longitudinal and horizontal shear stresses even more imperative.

To account for the geographic variation of sediment cover, we derive a till factor ($f_b(x, y)$ in Eq. (5)) from the sediment thickness map of Laske and Masters (1997) as shown in Fig. 1. The till factor was obtained by dividing the actual till depth by 20 m, setting the till factor to 0 for till depths below 5 m, and limiting the value of the till factor to 1. In addition, the model imposes unit till factor for all present-day regions with bathymetry deeper than 20 m. Based upon initial ensembles analyses, we found best fits to the constraints with till deformation inhibited for values of the till factor below 0.6 and we therefore also retain this cutoff for the present model simulations.

An exponent 3 Weertman-type sliding law (Tarasov and Peltier, 1999) with a moderate sliding parameter (Table 2) is also incorporated into this basal processes model. The model, furthermore, does not incorporate explicit ice-shelf dynamics. Instead, as a simple approximation, we smoothly impose a strong linear sliding law whenever ice approaches buoyancy with a sliding parameter of 0.07 Pa^{-1} m yr^{-1}. To increase numerical stability and allow for sub-grid heterogeneity, all basal sliding and till deformation is smoothly introduced beginning at 0.25°C below the pressure melting point.

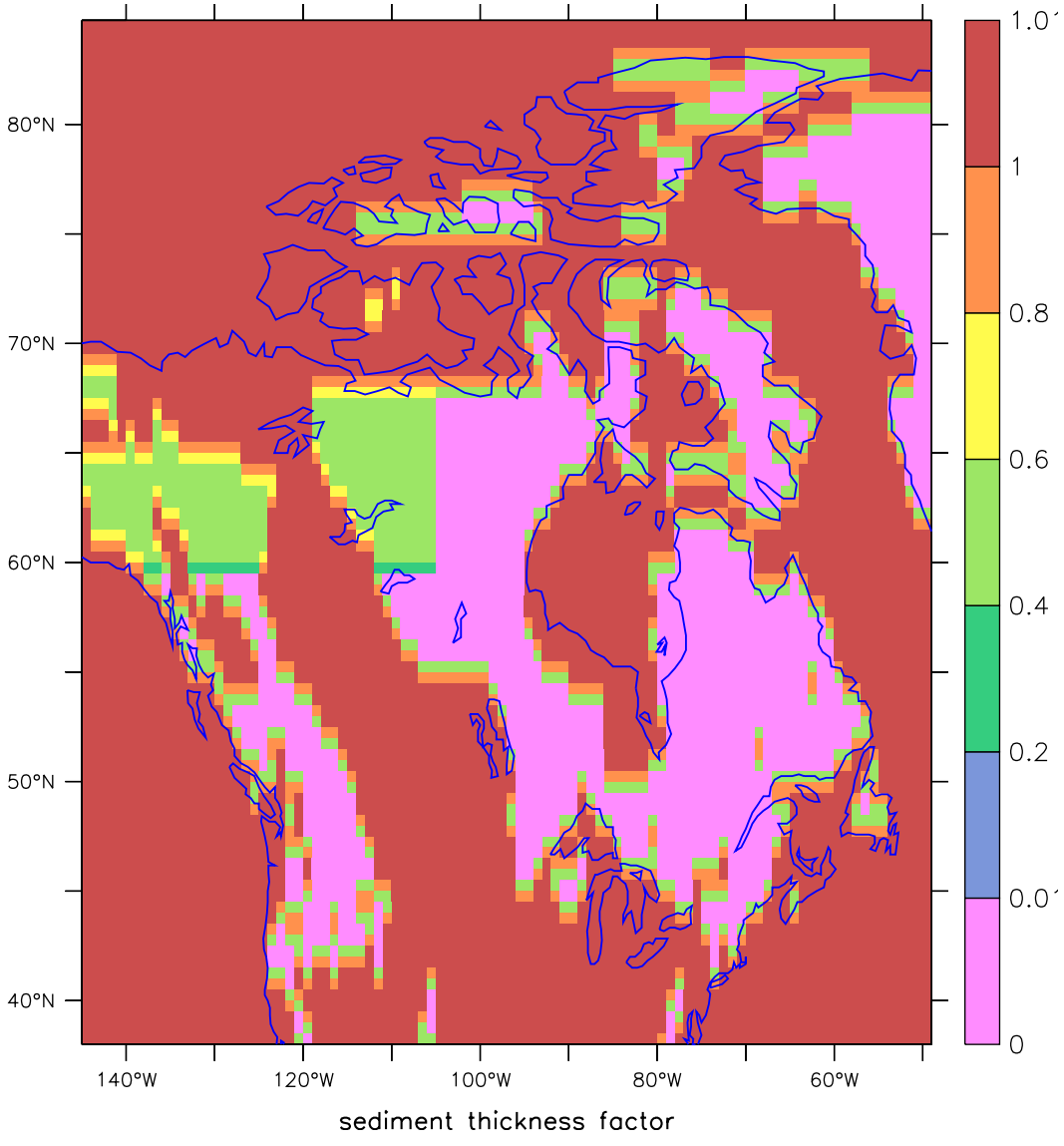

Fig. 1. Till-deformation factor map for the NA Continent.

2.4. Bedrock response and RSL computation

Bedrock response to surface load variations is computed on the basis of a linear viscoelastic field theory for a spherically symmetric Maxwell model of the earth (Peltier, 1974, 1976). The bedrock displacement $R(\theta,\psi,t)$ is determined from a space-time convolution of the surface load per unit area $L(\theta,\Psi,t)$ with a radial displacement Greens function $\Gamma(\gamma,t-t')$ (Peltier, 1974), in which γ is the angular separation between source point and field point as

$$R(\theta,\psi,t)=\int_{-\infty}^{t}\int\int_{\Omega}L(\theta',\psi',t')\Gamma(\gamma,t-t')\,\mathrm{d}\Omega'\,\mathrm{d}t'. \quad (6)$$

The radial viscosity profile is represented by that of the VM2 model (Peltier, 1996; Peltier and Jiang, 1996) with a 100 km thick lithosphere and the PREM model (Dziewonski and Anderson, 1981) is assumed to describe the radial elastic structure. The convolution integral is evaluated spectrally using the methodology of Peltier (1976) with truncation at degree and order 256. Bedrock response is asynchronously coupled to the ISM at 100 yr time steps. The model is initialized during the Eemian interglacial at −122 kyr with the present-day observed surface and bedrock topography assuming isostatic equilibrium at that time. A truncated northwestern Greenland ice sheet is also included to allow glaciation across Nares Strait (between Greenland and Ellesmere Island). The marine component of the surface load, for the purpose of integrating the ice dynamics model, is computed using an eustatic approximation.

Model RSL histories are post-processed using the gravitationally self-consistent theory most recently described in Peltier (1998b). The RSL tuned model GrB (Tarasov and Peltier, 2002) provides the Greenland component of the load history and ICE-4G (Peltier, 1994) is used to provide the remaining load histories (i.e. aside from that for NA). As post-process "implicit ice" load corrections (Peltier, 1998a) make no sense in the present context, we use an ocean mask fixed to present-day geography and reduce the ice load by the contemporaneous eustatic water load (as computed by the ISM) up to a maximum equivalent to ice flotation. This approach largely accounts for the impact of a changing ocean mask that is required for topographic self-consistency. Furthermore, it avoids type II implicit ice corrections that are required when a changing ocean mask causes sudden inundation of a region that was previously ice covered. It should also be noted that type I implicit ice corrections (Peltier, 1994) are negligible for load histories that start at inception (and therefore do not assume isostatic equilibrium at LGM). As shown in Fig. 2, the imposition of topographic self-consistency on the RSL computation (i.e. computed with a time-varying ice mask shown as a long-dashed curve) has generally a minor impact relative to RSL observational uncertainties. However, the eustatic water load corrections have the most significant effect (solid line in Fig. 2). Unlike many past geophysical analyses, the RSL computation also includes the full influence of the load history back to the Eemian at −122 kyr so that isostatic equilibrium is not assumed at LGM. However, for at least one of our best-fit models (nn2016), this has insignificant impact. It should be noted that inclusion of full load histories would be important for models which have much more isostatic disequilibrium at LGM. When applied to model nn2016, the four different RSL computations (i.e. with and without the imposition of topographic self-consistency (Peltier, 1994) based on the assumption of isostatic equilibrium at LGM, and with and without eustatic load corrections using the full glacial cycle history) did not differ significantly for all of the other primary RSL sites that are not shown in Fig. 2.

2.5. Climate and margin forcing

Climate forcing is arguably the component of glacial cycle models that is most difficult to constrain. Given the uncertainties derivative of the poor quality of the constraints that are available, climate-related parameters consume 16 of the 20 ensemble parameters listed in Table 1. For the present work, we will use an inferred temperature history for the Greenland summit region to provide a glacial index, $I(t)$, to interpolate between observed present-day and LGM climate fields over NA derived from a composite of the PMIP archived −21 kyr simulations (http://www-lsce.cea.fr/pmip/index.html). Specifically, using the GRIP $\delta^{18}O$ record and the observed value for the $\delta^{18}O$ lapse rate in central Greenland of $\lambda_\delta = -6.2\ \mathrm{mil}^{-1}\ \mathrm{m}^{-1}$ (Johnsen et al., 1989), we define this glacial index as

$$I(t)=\frac{(\delta^{18}O(t)-\delta^{18}O(0)-\lambda_\delta(h_{GRIP}(t)-h_{GRIP}(0)))}{(\delta^{18}O(LGM)-\delta^{18}O(0)-\lambda_\delta(h_{GRIP}(LGM)-h_{GRIP}(0)))} \quad (7)$$

with the surface elevation of GRIP ($h_{GRIP}(t)$) taken from the tuned model (GrB) of Tarasov and Peltier (2003). In order to better fit the inferred rate of glaciation during inception, we found it necessary to add 0.2 to the index from −117 to −112 kyr. A recent study (Marshall, 2002) using a similar glacial index forcing and with sub-grid topographic and glaciological parameterizations (to compensate for mass-balance sensitivities to topographic and model resolution) also found that extra cooling was necessary to obtain an inception rate for ice growth corresponding to that inferred on the basis of deep sea sedimentary $\delta^{18}O$ records.

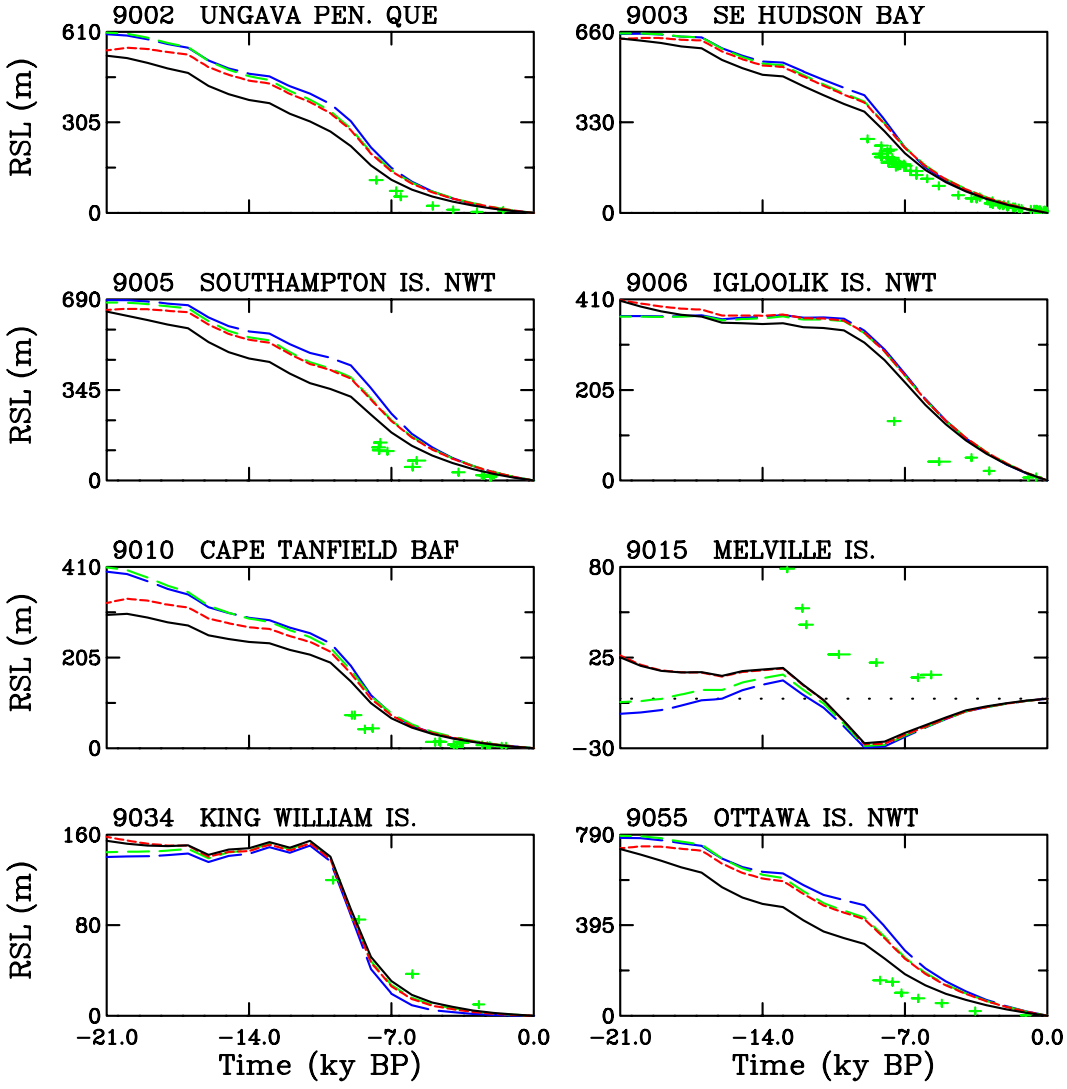

Fig. 2. Comparison of post-process RSL computations for most sensitive RSL sites using model nn2016 (described in detail in what follows). Long-dashed blue curve is for topographically self-consistent time-dependent ocean mask, while the medium-dashed green curve is for ocean mask fixed to present day, both with assumed isostatic equilibrium at LGM. Short-dashed red curve uses full glacial cycle load history, while solid black curve additionally uses eustatic load correction to explicitly account for implicit ice. Numbers adjacent to the names of the individual sites are those in the University of Toronto RSL data base.

Sea-level temperature fields (T_s) are interpolated between modern and LGM climates using the glacial index as

$$T_s(\mathbf{r},t) = I(t)T_s(\mathbf{r},\mathrm{LGM}) + (1 - I(t))T_s(\mathbf{r},0). \quad (8)$$

The present-day climatology ($T_s(\mathbf{r},0)$) is derived from a 14 yr mean (1982–1995) of reanalyzed 2 m monthly mean temperature fields (Kalnay, e.a., 1996). A 7.5°C km^{-1} environmental lapse rate is used to adjust surface temperature to contemporaneous surface elevation.

Based on the exponential nature of the dependence of saturation vapor pressure on temperature, precipitation is exponentially interpolated between the present-day observed climatology $P(0,x,y)$ (Legates and Willmott, 1990) and LGM field from the PMIP ensemble $P(\mathrm{LGM},x,y)$ using the following expression:

$$P(t,x,y) = \mathrm{RP_{SM}}(t,x,y)P(0,x,y) \times \left\{\frac{\mathrm{fP_W}(t,x,y)fPP(\mathrm{LGM},x,y)}{P(0,x,y)}\right\}^{I(t)^{\Theta_P}}. \quad (9)$$

The "ensemble phase factor" (Θ_P) is introduced to parameterize some of the uncertainty associated with the transition from interglacial to glacial atmospheric states, while fP is a global ensemble scale parameter. Two additional ensemble scale parameters ($\mathrm{RP_{SM}}$ and $\mathrm{fP_W}$) allow for regional enhancements during the −30 to −10.6 kyr period. This was found necessary in order to improve fits to geophysical observations in Western and Southwestern Canada. The −30 kyr onset time for these regional modifications is assumed to follow glaciological

inferences of significant glacial expansion into the Keewatin/Alberta region (Dyke et al., 2002). It can be partially rationalized as being required to correct LGM GCM fields that were obtained from model runs lacking a significant Keewatin dome in their topographic boundary conditions. We hypothesize that the growth of such a dome, the existence of which has largely been confirmed in Peltier (2002a), diverted the jet stream southward, and baroclinic instability along the southern margin of the ice sheet thereafter enhanced regional precipitation. The −10.6 kyr termination of these regional modifications has been assumed so as to correspond to the approximate time of demise of the last remnant of the Keewatin dome.

Our attempts to specify an LGM climate state have gone through a number of iterations in order to best capture the uncertainties associated with current GCM simulations of glacial climate. In order to capture the inter-model variance of the PMIP set of LGM climate simulations, we define a base climate as a weighted average of the results of the five highest resolution models using a mixed-layer representation of the oceans (UGAMP, UKMO, CCC2, GFDL, GEN2) and the highest resolution model in which a specified sea-surface temperature field was employed (ECHAM3). The two highest resolution mixed-layer models (UGAMP, UKMO) were given a double weighting. Initially, we applied this specification to both surface temperature and precipitation–evaporation (P–E) fields. However, initial investigations found much improved results with a P–E field that was a simple average of the three highest resolution mixed-layer models (UGAMP, UKMO, CCC2).

We also incorporate empirical orthogonal basis functions among the ensemble parameters to capture the inter-model variance of the six GCMs. The first two EOFs for precipitation and the first three EOFs for temperature capture, respectively 66% and 78%, of the total variation. We include these five EOFs using five ensemble parameters that range over 150% of the range of the EOF coefficients for the PMIP ensemble. Inclusion of the next most relevant EOF increased capture to 81% and 90% of total inter-model variation for precipitation and temperature, respectively. However, analyses with neural network models determined that these extra components had very low relevancy (Tarasov et al., in preparation).

A previous ensemble-based analysis of NA ice complex evolution (Marshall et al., 2002) led to the conclusion that the parameterization of a desert-elevation effect was the most sensitive determinant of ice-sheet form in their model. The desert-elevation effect was first included in continental ice-sheet simulations by Budd and Smith (1981) on the basis of observations in Antarctica. Climatologically, it may be seen to be acting so as to correct GCM precipitation fields for the higher surface elevations arising with the high-resolution grid of the ISM, with precipitation reductions following the decrease in saturation vapor pressure with temperature. However, in order to improve fits to the RSL observations, we have found it necessary to incorporate much stronger regional desert-elevation cutoff factors than can be justified on the basis of saturation vapor pressure changes. These strong cutoffs can be interpreted as parameterizing the impact of the above-mentioned atmospheric reorganization due to the presence of the large Keewatin dome, a feature that was not included in the topographic boundary conditions of the PMIP simulations of LGM climate that are employed herein to represent glacial conditions. In keeping with our atmospheric reorganization hypothesis, these regional cutoffs are imposed only during the −30 to −10.6 kyr period when a significant Keewatin dome was found to be present in preliminary ensemble analyses.

The use of a single climate proxy index based upon the Greenland Summit $\delta^{18}O$ record together with the above-defined "phase factor" is highly unlikely to allow us to capture the complexities of deglacial climate change over NA. Climate has three impacts on an ice sheet. Firstly, it is a primary control on margin position. Summer surface temperature is most critical in this regard, especially on sub-millennial time scales. Secondly, over the interior region of the ice sheet, precipitation determines surface mass balance. This has a direct impact on interior topography. Thirdly, mean yearly temperature and precipitation impact ice temperature and therefore flow dynamics. This effect is, however, subject to lags determined by vertical velocities which, interior to the ice sheet, can be approximated to first order by means precipitation rates, and are therefore of order 0.1 to 0.3 m yr^{-1}. Since it is only the near basal ice temperatures that have significant impact on ice flow, uncertainties in climate during the deglacial period will have only a small impact on ice rheology. Much of the impact of climate on deglaciation therefore relates to margin position. The availability of a recently constructed high-resolution digitized margin chronology (Dyke, 2003; Dyke et al., 2003) can therefore allow us to significantly reduce model system uncertainties associated with deglacial climate. The new chronology (Fig. 3) has varying time slices during the deglacial period (50–900 yr time steps) and starts at −21.4 kyr. Ideally, one might imagine introducing a sufficient number of ensemble parameters into the climate parameterization to enable us to employ the margin chronology to infer an appropriate climate history. However, computational limitations will rule out such an approach for the foreseeable future.

Instead, we will directly impose the inferred ^{14}C controlled margin chronology (using the INTCAL98 ^{14}C to calendar year conversion of Stuiver et al., 1998) through modifications to the surface mass balance. To

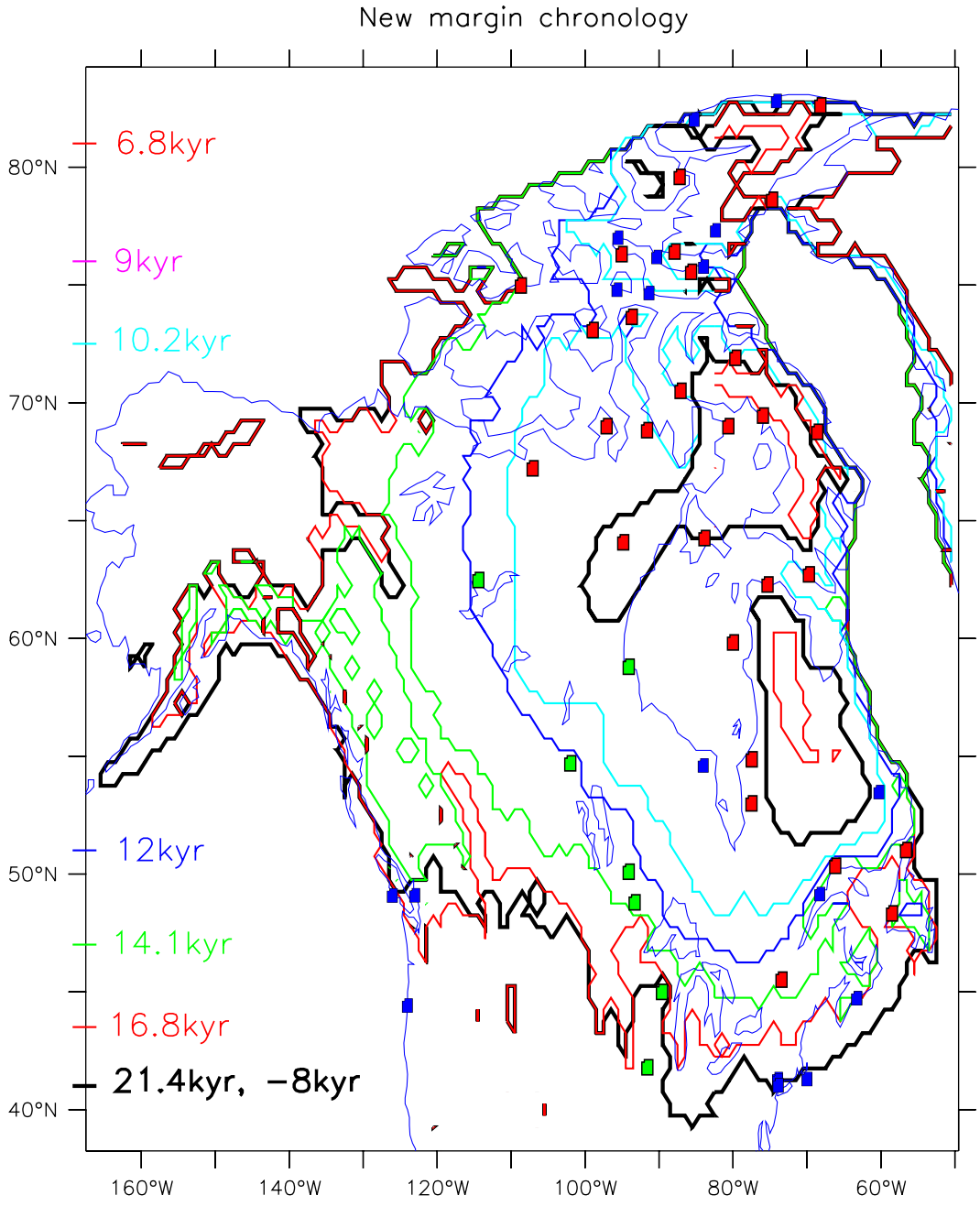

Fig. 3. Margin forcing chronology (calendar years) from Dyke et al. (2003) with only eight of the 36 available time slices shown. Also shown are primary and secondary RSL sites (red and blue, respectively) and sites for which geodetic and absolute gravity observations are also available (green).

allow for margin chronology uncertainties and short-term ice surges, we attach to the digitized chronology an approximately ± 100 km buffer zone (subject to model grid-point resolution) around the inferred margin. Interior to this buffer zone, if ice thickness is less than 300 m, ablation is eliminated and accumulation is further enhanced (to a maximum of 0.3 m yr^{-1}) if ice thickness falls below 100 m. Furthermore, ablation is also eliminated from regions more than two grid points interior to the buffer region. Regions outside the margin were originally assumed to be at least in the ablation zone if not ice free. However, initial ensemble studies that varied the increase in ablation across the outer buffer zone required high ablation rates and effectively ice-free conditions in the outer buffer zone to better fit the RSL constraints. For this reason, for ice-covered grid boxes outside the inferred margin, ablation is currently set to 40 m yr^{-1}. Margin forcing is smoothly interpolated between digitized time slices and is also smoothly introduced beginning at 1.5 kyr prior to the first time slice (−21.4 kyr) of the digital chronology. Given that the geological evidence indicates that most

regions of the ice sheet reached full margin extent by about 4 kyr prior to LGM (Dyke et al., 2002), our 1.5 kyr onset period is, if anything, overly short. A short onset period was chosen so as to allow investigation of the maximum extent to which isostatic disequilibrium at LGM might "contaminate" the geophysical inversion of RSL data.

Initial ensemble analyses led to the conclusion that full margin forcing was too restrictive with respect to obtaining acceptable fits to the RSL observations. Given that glaciological observations provide only weak constraints on past marine margin locations and that they are especially hard pressed to distinguish between ice shelves and grounded ice, we allow ice calving to over-ride the margin chronology (which obviously only occurs in the marine sectors of the ice sheet). As will be demonstrated below, this proves to be critical for the purpose of obtaining acceptable model fits to the RSL data in the Arctic region.

2.6. Geophysical data

The recently updated University of Toronto global RSL database contains data from over 500 sites for NA alone. However, in order to reduce both computational and conceptual complexity for the purpose of this initial analysis, we have chosen to use a geographically disperse subset of 28 primary sites containing high-quality internally consistent data to define the RSL constraints for the model (Fig. 4). RSL data from an additional 24 sites have also been included to provide independent validation of the constrained model.

A key limitation of RSL data from previously ice-covered sites is that it is only available from locations that had been previously inundated by the sea and that are now exposed land. Clearly, the continental interior of Western Canada is a region devoid of RSL constraints. It is therefore fortunate that a variety of modern geophysical observations have recently become available for this region. Results from Very Long Baseline Interferometry (VLBI), in particular, have delivered a measurement of the present-day rate of vertical motion of 8 ± 1.5 mm yr^{-1} at Yellowknife (Argus et al., 1999) (labelled Y in Fig. 4). Furthermore, a recently completed transect of repeated absolute gravity measurements (Lambert et al., 2001) has provided measurements of the time derivative of the surface gravitational acceleration ($\dot{g}$) for the south-central region of the Laurentide Ice Sheet (these sites are denoted by lowercase letters in Fig. 4). Taken together, these new geophysical measurements provide significant coverage of a region that was previously unconstrained. They are also critical to recent geophysical arguments for the existence of a Keewatin Dome on the Canadian Shield to the west of Hudson Bay (Peltier, 2002a). As shown in Fig. 4, the RSL and geodetic data together offer reasonably complete (though regionally sparse) geographic coverage of the regions that were previously ice covered.

3. Analyses and results

We first performed a set of 900 runs of the glacial systems model with ensemble parameters randomly sampled over the ranges specified in Table 1. This initial ensemble delivered NA ice sheets with corresponding contributions to the eustatic sea-level fall at LGM that ranged from near 0 to about 105 m, attesting to the wide coverage of the parameter space provided by these initial ranges. Subsequently, a further 300 runs were completed with parameter ranges reduced to capture best-fit regions of the parameter space (using the metric described below applied to the initial 900 runs). It should be noted that when referring to ensemble results "LGM" is taken to be -20 kyr, otherwise LGM is generally taken to be the -22 to -19.5 kyr period. In what follows, we will first examine results for the ensemble as a whole, then focus upon a few best-fit cases and finally examine model constraints on the contribution to eustatic sea-level change from NA during deglaciation.

3.1. Ensemble results

Examination of a large ensemble of results requires definition of at least one metric to measure goodness of fit. We have chosen to use the root-mean-square (RMS) error over our calibration subset of 28 RSL sites, six $\dot{g}$ sites, and the Yellowknife $\dot{R}$ site. Given that most RSL data points represent a minimum estimate of the actual contemporaneous sea level, negative RSL discrepancies (i.e. model prediction below observed and outside of data-point error bars) are given a factor 5 error weighting. RSL errors are computed using observed RSL data points (i.e. no RSL envelope is assumed and all data points for a site are weighted equally). To avoid bias due to the large geographic variation in the magnitude of the RSL response to the glaciation–deglaciation process, RMS errors at individual RSL, $\dot{g}$, and $\dot{R}$ sites are normalized by the ensemble RMS error for that site. Furthermore, on the basis of their critical location, RMS errors for the 9004, 9005, 9055 RSL sites (Fig. 4, the first two digits of the site numbers from the RSL database are suppressed on this map) and for the $\dot{R}$ site are given a double weighting, while RSL site 9003 (southeast Hudson Bay) is given a factor five weighting due both to its critical location and to its exceptional data quality, as discussed in detail in Peltier (1998b).

To ease interpretation, we further apply two data "sieves" to the ensemble results. The first sieve imposes the following three conditions: (1) present-day uplift at

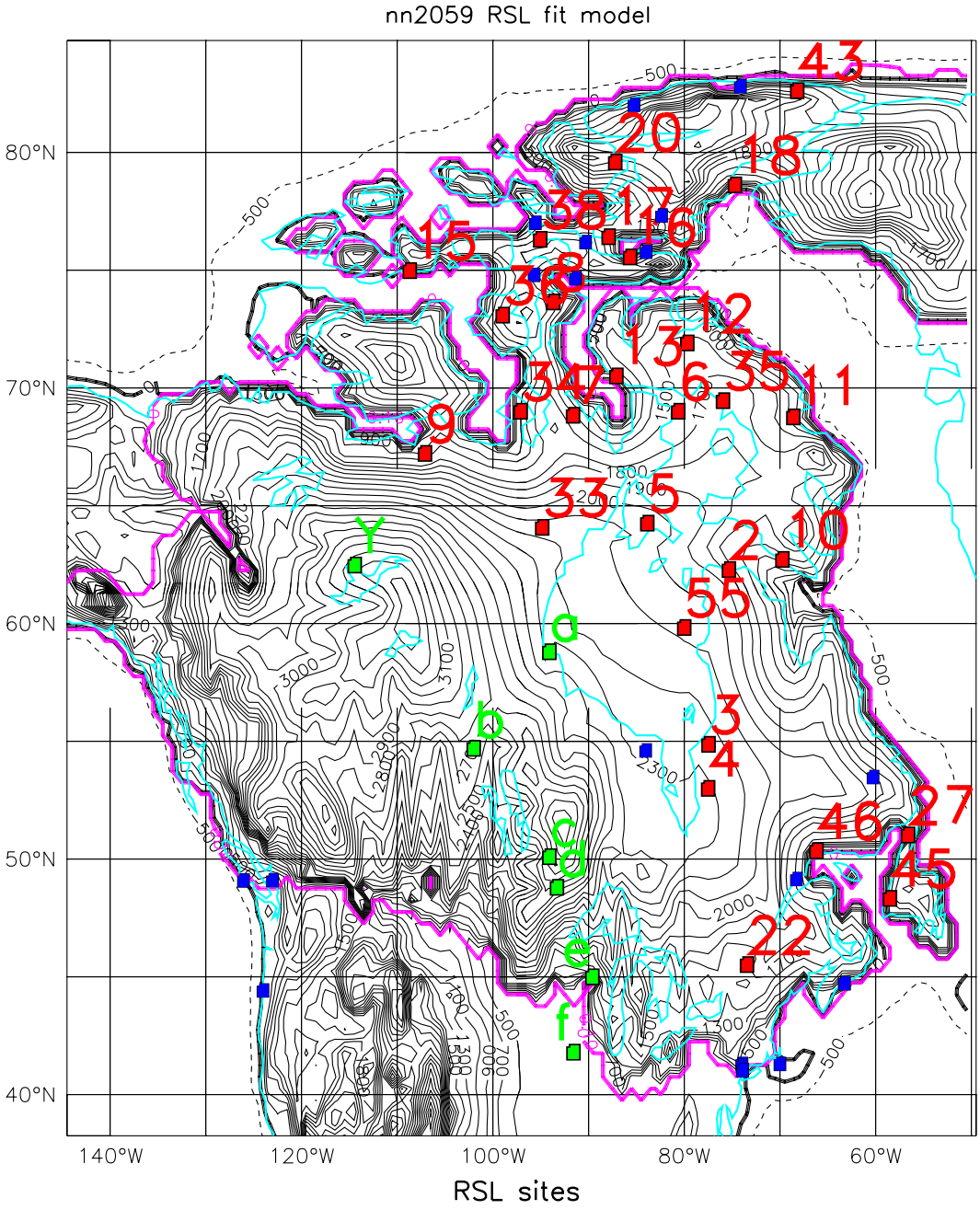

Fig. 4. Site map for ensemble constraints. Primary RSL sites are shown numbered in red. Secondary RSL sites are in blue and present-day uplift and time derivative of surface gravitation acceleration sites are shown in green. The LGM surface topography is that of the best-fit model nn2059 to be discussed in what follows.

Yellowknife is within the range of observational uncertainty (8 ± 1.5 mm yr^{-1}), (2) Hudson Bay is completely ice covered at -26 kyr, and (3) ice area at -26 kyr is within 20% of inferred LGM extent. Condition two is justified on the basis of Heinrich event 2 data which are interpreted to suggest that Hudson Strait was fully glaciated to the sill near the mouth of the Strait just prior to LGM (Dyke et al., 2002; A.S. Dyke, per. comm., 2003). Without this ice-cover constraint, best fits to the RSL constraints for the Hudson Bay region were obtained for models with incomplete Hudson Bay ice cover at -24 kyr. In hindsight, it is arguable that -26 kyr is a bit premature, and in ongoing work we have moved the requirement for full ice cover over Hudson Bay to -25 kyr. However, ongoing ensemble analyses using a much more refined calibration procedure mostly produce full ice cover at -26 kyr for models that have full ice cover at -25 kyr (with, for instance, two exceptions in a recent ensemble of 200 runs). Furthermore, though there is evidence for

open-water conditions over Hudson Strait prior to −26 kyr (Andrews and MacLean, 2003), we are not aware of evidence for such conditions between −26 kyr and LGM. From a dynamical point of view, the interpretation of Heinrich event 2 as being associated with a large ice stream through Hudson Strait would argue for near-complete glaciation of Hudson Bay much earlier than −26 kyr. Otherwise, it would be very difficult to obtain the large amount of temperate (or near-temperate) ice required to feed such an ice stream.

Geological inferences to the effect that most of the ice sheet had reached maximal extent by 4 kyr prior to LGM (Dyke et al., 2002) justify condition three. The application of this first sieve selects 276 runs from the total of 1200 ensemble runs. The second sieve thereafter selects the top 20% of models passing the first sieve (56 models) with respect to the total normalized mean-square error for all RSL data points and other geophysical observations.

The first issue we will examine relates to the existence of an ice dome in the southeast sector of the ice sheet over north-central Quebec. To quantify the topographic distinctness of such a dome, we define a dome separation metric for the region given by the maximum ice surface elevation east of 80° W longitude in Quebec/Labrador minus the maximum ice surface elevation for a transect running south from James Bay at 80°W longitude. Fig. 5 reveals a strong anti-correlation between ensemble dome separation and RSL error for site 9003 (southeast Hudson Bay) for the sieved subsets. Extrapolation of the displayed relationship would suggest that a best fit to the site 9003 RSL data would require a southeast dome that rose close to 400 m above the peak of the ice ridge along the 80°W longitude transect. As to the physical properties of the model that supports the existence of this dome, the ensemble parameter that is correlated most strongly with dome separation is that for till viscosity (Fig. 5). Aside from a few outliers from the primary sieve (and none of the secondary sieve), strong dome separation requires low till viscosity to produce fast ice flow. Also evident in Fig. 5 is that aside from two outliers, all secondary sieve sub-ensemble members have low till viscosity (below $10^{9.9}$ Pa s) and thus strong till deformation. A positive correlation between RSL fit and strong till deformation was also observed in all prior ensembles (not shown).

It has also become clear in our analyses of ensemble results that it is not simply fast flows but specifically fast flows due to till deformation that are critical for determining LGM ice topography. Flow-line model reconstructions of the Laurentide Ice Sheet (Clark et al., 1996b) have also invoked strong till deformation to obtain the aspect ratio of the geophysically constrained ICE-4G model of Peltier (1994). To illustrate the critical role of till deformation, we have subjected one of the

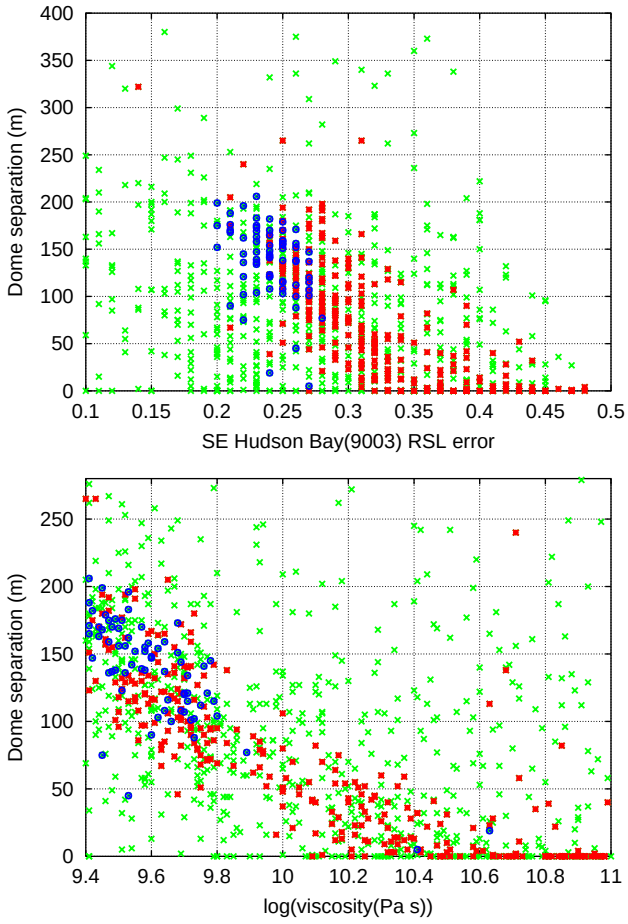

Fig. 5. Ensemble southeast dome separation versus southeast Hudson Bay RSL error and till viscosity. Runs that passed the secondary sieve are indicated by dark blue circles, while runs that only passed the primary sieve are indicated by medium dark red boxes.

better fitting ensemble members (model nn1164) to a number of flow modifications (Fig. 6). This model is distinguished by having a fast-flow structure consistent with geological inferences (Stokes and Clark, 2001; Dyke et al., 2002), i.e. it has a well-defined Lancaster Sound ice stream fed by a stream running east from the M'Clintock channel (draining into the Lancaster Sound ice stream, though displaced southward from its inferred Prince of Wales Island location), as well as Smith Sound (draining Nares Strait), Hudson Strait, and coastal British Columbia ice streams with maximum velocities of approximately 2.5, 4, 3, and 4 km yr^{-1}, respectively. Two other significant LGM ice streams in the model (the Des Moines ice stream running south from Lake Winnipeg and a M'Clintock channel ice stream running north from Victoria Island) have also been geologically inferred, but only for the post-LGM period (Stokes and Clark, 2001).

Most of the ice streams in this base model are generally one grid point in width. This is largely a

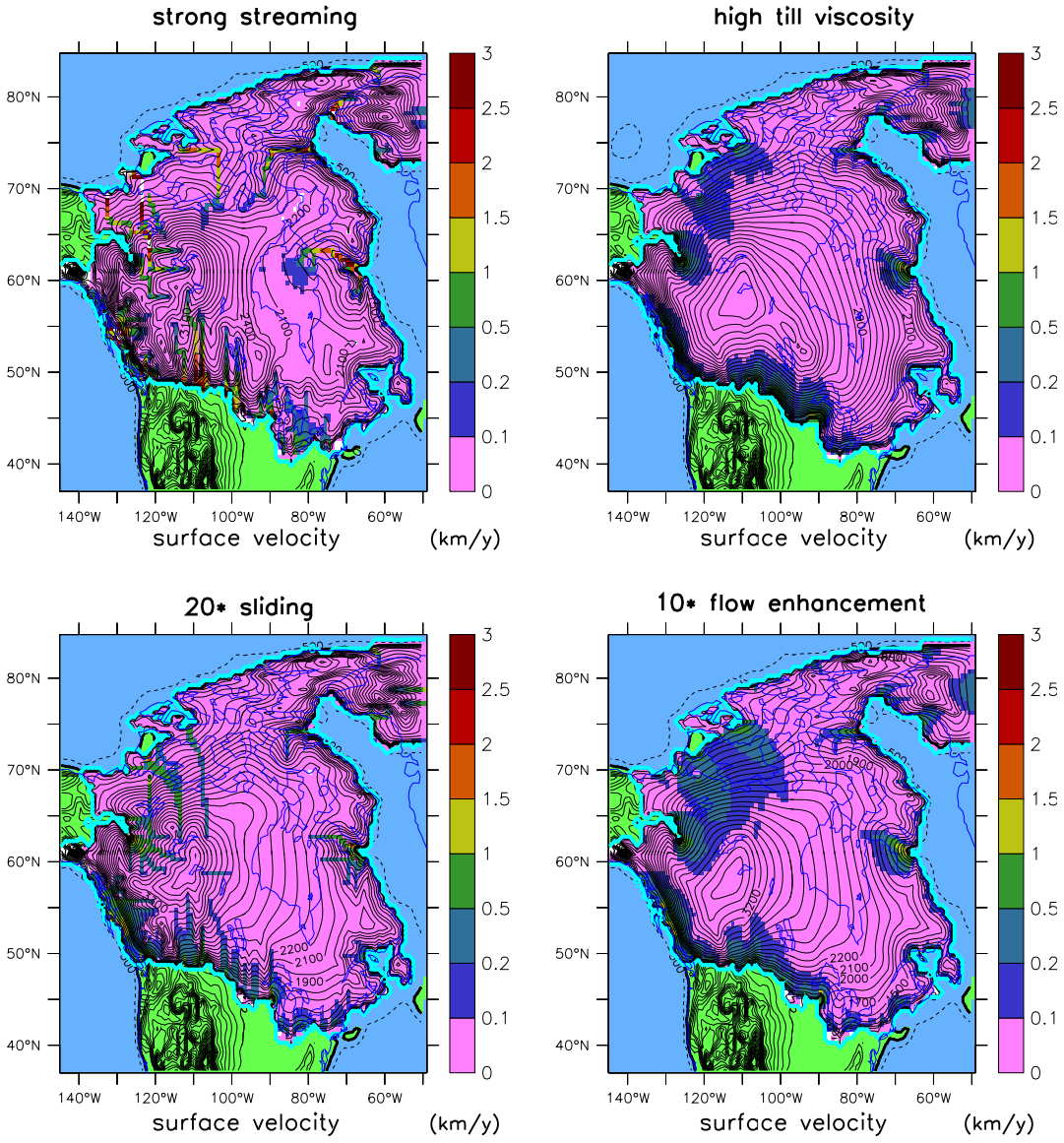

Fig. 6. Comparison of LGM ice sheets for different fast-flow mechanisms. All models aside from the strong streaming model have high till viscosity.

consequence of thermodynamic control as basal temperatures are generally below the pressure melting point in the grid boxes adjacent to these narrow streams (not shown). This "thermostealing" mechanism has been previously observed in models with fast basal flows (Payne and Dongelmans, 1997) and appears to result from a positive feedback between basal flow velocity and basal heat generation, tempered by a negative feedback arising from advection of colder ice into the adjacent grid cells.

The strong Hudson Strait streaming in the base model produces significant drawdown of Hudson Bay ice. This, together with wide-spread streaming over the south-eastern lobe (southern Ontario region), enables the topographic definition of the Quebec dome. Turning off till deformation via imposition of high till viscosity results in a mono-domed Laurentide/Cordilleran ice sheet at LGM and leads to a 34% increase in LGM ice volume (Fig. 6). If we then subject this high-viscosity model to a 20 fold increase in the sliding parameter, we obtain a model with only a 10% increase in ice volume (relative to nn1164). Although this high-sliding model has a small residual dome over Labrador due to the ice incision from the open Gulf of Saint Lawrence, the general topographic structure is very similar to the mono-domed slow flow model except for the reduced aspect ratio. Without the strong geographic control provided by sediment location, strong sliding is unable to concentrate fast flows in, for instance, the Hudson Strait and Lancaster Sound channels. The flow is thereby unable to significantly drawdown ice around Quebec/Labrador and thus lead to a well-defined southeastern dome. It is interesting to note, however, that the thermostealing mechanism appears to be

operative in Western Canada with the appearance of narrow ice streams in this region.

Imposing a 10 fold increase in the flow enhancement parameter on the slow flow model produces an LGM ice sheet with ice volume within 2% of the base model, but once more with a mono-domed structure (Fig. 6). The lack of fast-flow concentration is even more evident in this model. Furthermore, as described in Marshall et al. (2000), models with high (ice deformation) flow enhancement suffer from excessive cold advection to the base, thereby further limiting basal flows.

RSL constraints also appear to require strong drawdown of Hudson Bay ice. Model fits to regional RSL data appear to require ice that is as thin as possible over Hudson Bay (Fig. 7). In fact, the best model fits to RSL site 9003 occur for models with incomplete glaciation of Hudson Bay at −26 kyr (which thereby fail the primary sieve). Extrapolation of results would indicate that a complete fit to the regional RSL data would limit maximum LGM ice thickness over Hudson Bay to only about 1.5 km (Fig. 7). As indicated by the gap in Fig. 7, this is very likely glaciologically untenable. No models passing the sieve conditions exist with maximum LGM ice thickness below about 2.4 km. It would also be difficult to envision how such a thin ice core could be sustained given the surrounding ice extent. Instead, as will be shown in the next section, this need for thin ice is likely at least partially due to insufficient Hudson Bay ice drawdown during Heinrich events H1 and H0 in the ensemble (and possibly due to the absence of an explicit accounting for an "outburst flood" of water from beneath the ice sheet that could have been responsible for some component of melt-water pulse 1a (mwp1a); see Peltier, 2003 for discussion).

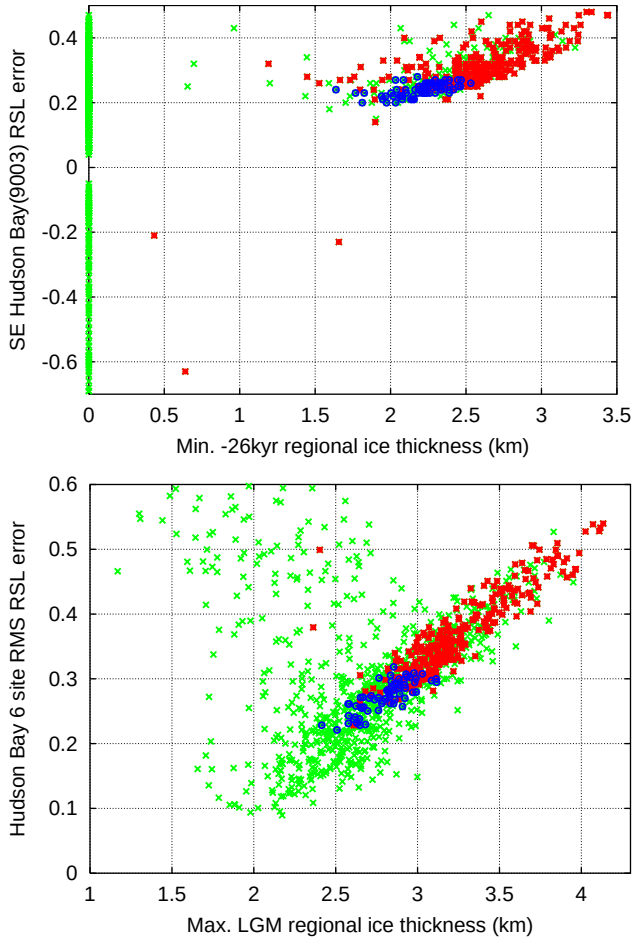

Fig. 7. Ensemble Hudson Bay RSL error versus regional ice thickness. Sieve correspondence is as for Fig. 5.

The $\dot{g}$ constraints (Fig. 4) further complicate model fits to Hudson Bay RSL data. Model fits to the $\dot{g}$ data require strong regional ice loading, resulting in a thick ice ridge running from the Keewatin dome down to the Great Lakes (Fig. 4). This thick ice ridge makes it more difficult to obtain thin ice over southern Hudson Bay. The ridge also comes close enough to directly affect the RSL chronologies of the southeast Hudson Bay region and the James Bay site (9003–9004), thereby requiring even thinner ice over Hudson Bay. Assuming that reported error bars on the observations are correct, the $\dot{g}$ values for locations "b" and "d" in Fig. 4 (Flin Flon, Man. and International Falls, Minn.) could not be fully reconciled with the model and margin forcing chronology. Runs with the best fits to the $\dot{g}$ measurements had $\dot{g}$ values that were low by approximately 0.23 and 0.08 mgals kyr^{-1}, respectively, for the two sites. Improved fits would require an even thicker ice ridge (difficult to obtain with the propensity for regional fast ice flow) and/or possibly thinner ice over southwest Hudson Bay. A denser set of $\dot{g}$ measurements for the region and improved error bars would be useful for clarifying the situation here.

RSL data from the north-central region of the ice complex in the vicinity of Lancaster Sound and south towards the Gulf of Boothia also proved difficult to fit (Fig. 8). Best fits were again achieved for ensemble runs that did not pass the primary sieve. The maximum velocity shown in Fig. 8 was computed across a diagnostic north–south transect across the Sound at −86.5° W longitude. Runs that had open water along this transect are indicated by very low maximum velocities (which then recorded ice velocities along the shoreline). Best fits were only achieved for model runs that had strong calving which maintained ice-free conditions in the Sound extending to the Gulf of Boothia, as for example, in Fig. 4. Since the calving parameters were global, these best-fit models also had excessive calving into Hudson Bay, thereby violating the primary sieve.

Aside from the constraints on global eustatic sea level, geophysical reconstructions that have relied purely on RSL data have been completely unconstrained over the interior of Western Canada (where no RSL data exists).

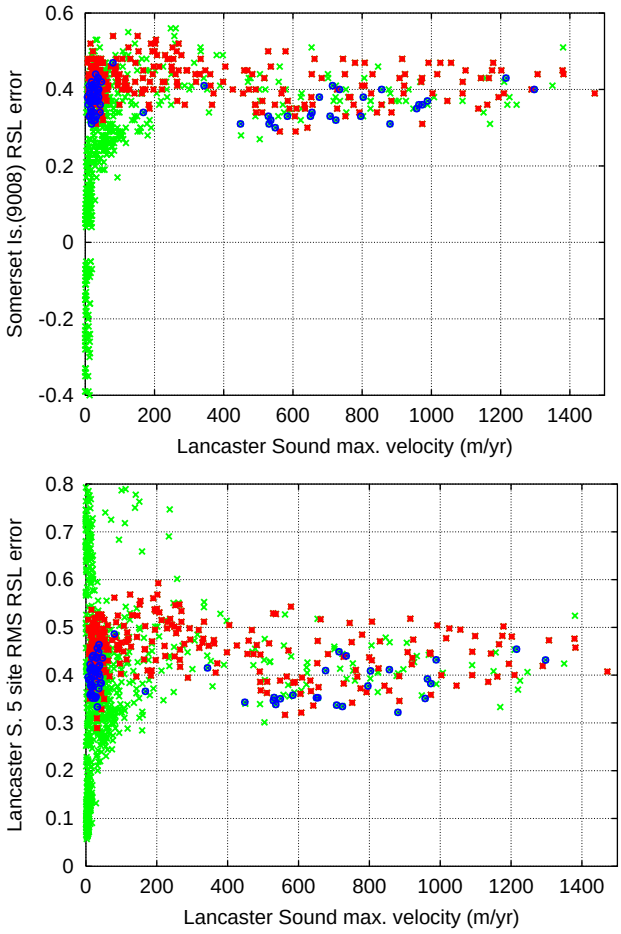

Fig. 8. Ensemble regional RSL errors versus maximum velocities (along −86.5° W longitude north–south transect) for Lancaster Sound.

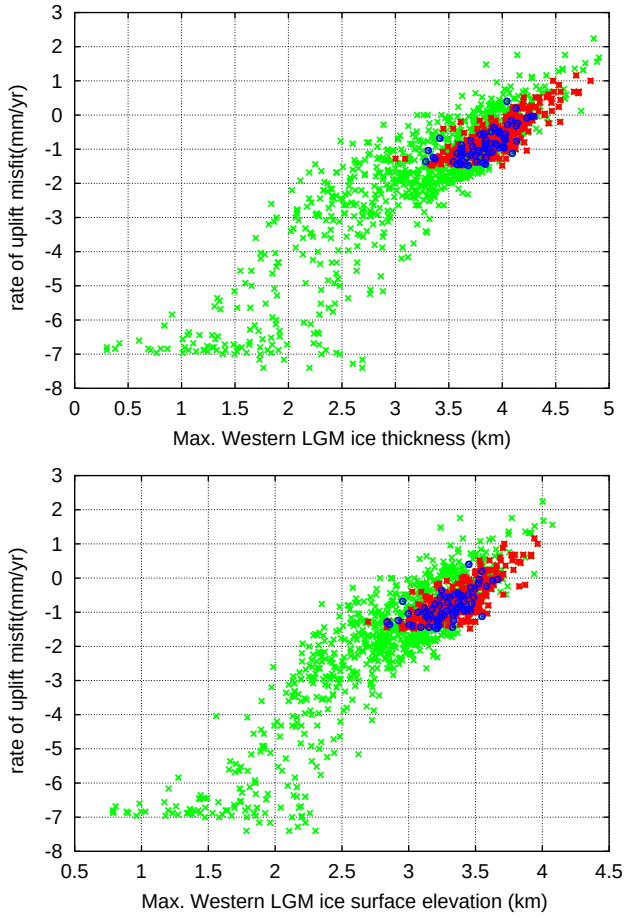

Fig. 9. Ensemble uplift rate misfit for Yellowknife versus maximum regional ice thickness and surface elevation.

The addition of the single present-day rate of uplift ($\dot{R}$) data point for Yellowknife, however, imposes a strong constraint on the region. Secondary sieved ensemble results suggest that maximum ice thickness in that region reached between 3.3 and 4.3 km, corresponding to a maximum surface elevation between 2.8 and 3.7 km (Fig. 9). Examination of Fig. 9 also indicates that a reduction in error bars for $\dot{R}$ at Yellowknife could significantly further constrain regional ice thickness.

In summary, ensemble results point towards an LGM ice sheet that had a large Keewatin dome and relatively thin ice in the east with strong drawdown over Hudson Bay and open-water conditions over Lancaster Sound extending south to the Gulf of Boothia. Glaciologically, aside from poorly constrained grounding-line conditions, the impact of open-water conditions on adjacent grounded ice is largely indistinguishable from the impact of ice-shelf coverage (especially at the current grid resolution). As such, open-water conditions in the modelled Arctic can also be interpreted as possibly representing ice-shelf coverage.

3.2. Best-fit models

We have endeavored to cover the true deglaciation history phase space for NA with only 20 parameters. However, upon completion of the ensemble of model runs, it became apparent that further modification of the model could significantly improve the fit to RSL observations.

Two key additions in this regard were the introduction of a separate calving temperature cutoff for the Arctic, and the incorporation of forced Heinrich event (H1 and H0) drawdowns of Hudson Bay ice (crudely implemented by limiting ice thickness to 1500 m during the −17.0 to −16.5 kyr period and to 1000 m during the −12.5 to −11.6 kyr period). The separate Arctic calving parameter permitted open-water conditions at LGM from Lancaster Sound to the mouth of the Gulf of Boothia and over M'Clintock channel down to Victoria Strait while maintaining glaciation of Hudson Bay and a strong ice stream in Hudson Strait (Fig. 4). With these modifications and some extra hand tuning, a significant improvement in fits to RSL observations was obtained

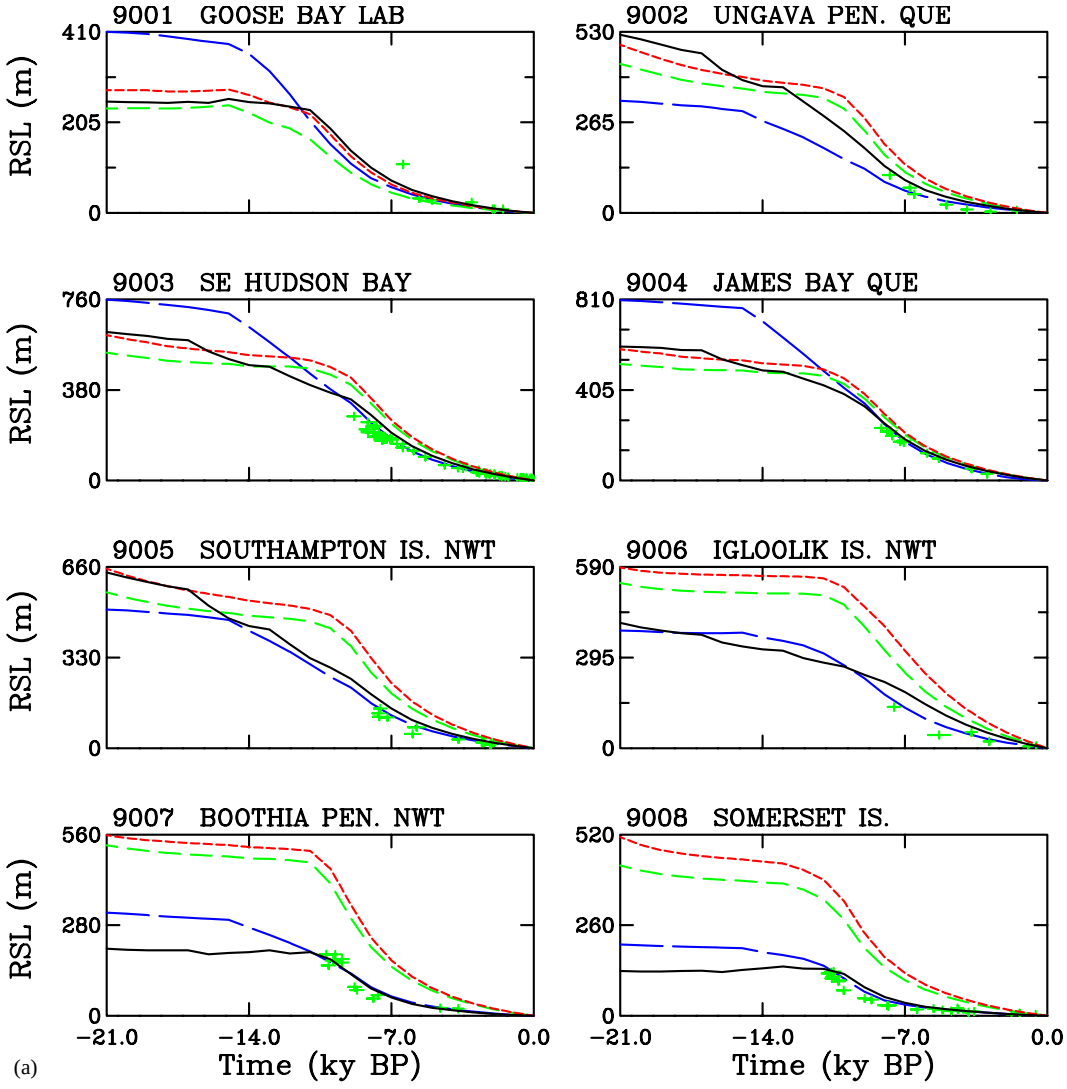

Fig. 10. RSL comparison of base models: ICE-4G (long dashed blue), nn9944 (best from ensemble, medium dashed green), nn1164 (fast flow, short dashed red), and nn2059 (hand tuned, solid black line): (a); (b); (c) and (d).

(Fig. 10) for what we here denote as model nn2059, which is compared to the best-fit model nn9944 from the ensemble.

The good fits at sites 9007–9008 and 9034 (Fig. 4) obtained for model nn2059 in comparison with the strong misfits for the other glaciological models displayed in Fig. 10 further substantiate the need for extensive open water (or ice shelves) in the Arctic during the LGM and post-LGM period. Fast ice streams can also reduce local ice loads. However, as is evident from the ensemble analyses above, even models with very strong ice streaming in Lancaster Sound (such as model nn1164 shown in Fig. 11) suffer from large misfits with respect to the regional RSL data (Fig. 10). The only other possible scenario that might fit the observations is a binge-purge process in which ice-stream marine termini repeatedly migrated up and down the Sound as has been hypothesized to occur in Hudson Strait during Heinrich events (MacAyeal, 1993). To approximately match the open-water conditions that the RSL constraints appear to favor, a dominance of purging (marine termini recession) over binging would likely be required under such a scenario, a circumstance that would be difficult to achieve dynamically.

Though the overall fit to the RSL data of the glaciologically unconstrained ICE-4G model is somewhat better than that of model nn2059, there are at least three sites (9009, 9027, 9045) where the fit of nn2059 is superior. The significant remaining misfits are due to excessive ice load (at LGM or during deglaciation) over the Foxe basin region to the west of Baffin Island (sites 9006 and 9035) and to a much lesser extent around Lancaster Sound (9016–17), regional misfits around Baffin Island (9010–11) and Ellesmere Island (9018 and 9020), and insufficient ice over the northwest Arctic in the vicinity of Melville island (9015). The predicted

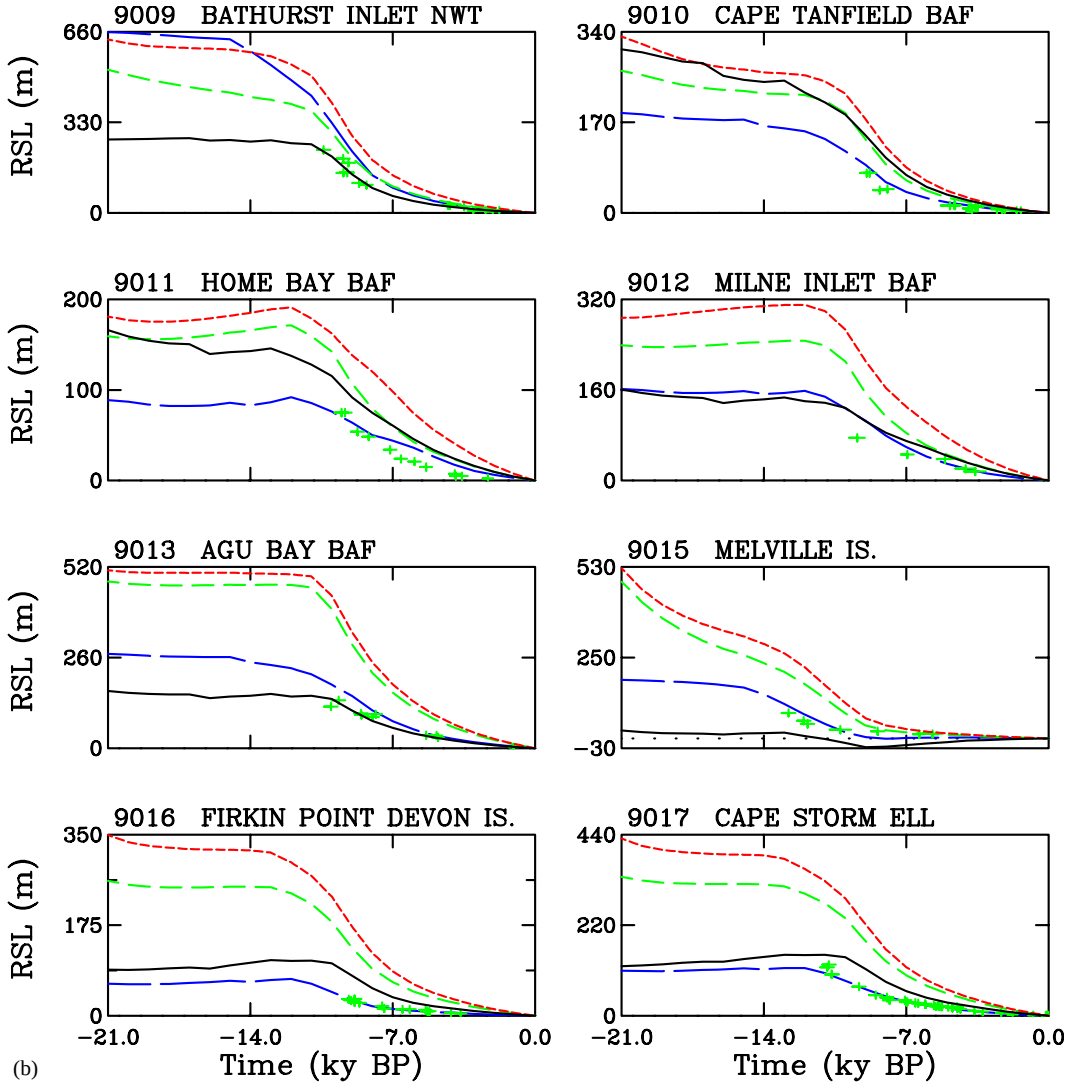

(b)

Fig. 10 (*continued*).

LGM ice cover over the latter region is highly sensitive to the calving parameter, and attempts at hand tuning resulted in either excessive or insufficient ice cover as indicated by model RSL chronologies. The misfit in the Foxe Basin, site 9006 (Igloolik), and to lesser extent at the Ipik Bay (9035) site, can be corrected with stronger Heinrich event (H1/H0) forcing for the Foxe Basin region (800 and 400 m ice thickness cutoffs for H1 and H0, respectively), but this resulted in open-water conditions over the Foxe Basin by −11 kyr. This is about two and half thousand years in advance of the margin chronology, which we have taken to be excessive. A future reevaluation of supporting data for the marine component of the margin chronology will be carried out to ascertain whether such an early deglaciation of Foxe Basin is acceptable.

Another possible means for improving RSL fits would be an enhanced mwp1a (from about −14.7 to about −14 kyr). However, a simple enhancement of the temperature forcing to present-day values (i.e. before adjusting for elevation) during this period has insignificant impact on the computed RSL chronologies for Hudson Bay and Foxe Basin (not shown). Even with such a strong climate forcing, surface temperatures in the interior region remain well below the freezing point due to the high elevation of the ice surface. Significant reduction of core region elevations over a relatively short time interval requires ice drawdown through fast flow and extensive ice calving. During this period, discharge of Hudson Bay and Foxe Dome ice would have had to occur through Hudson Strait. However, this is arguably ruled out by the lack of any paleo-oceanographic evidence for large-scale iceberg discharge from the strait during mwp1a. As such, we limit the imposition of forced Hudson Bay and Foxe Basin ice drawdown to the H1 and H0 periods.

The actual validity of such drastic H1/H0 drawdowns over Hudson Bay and Foxe Basin is difficult to

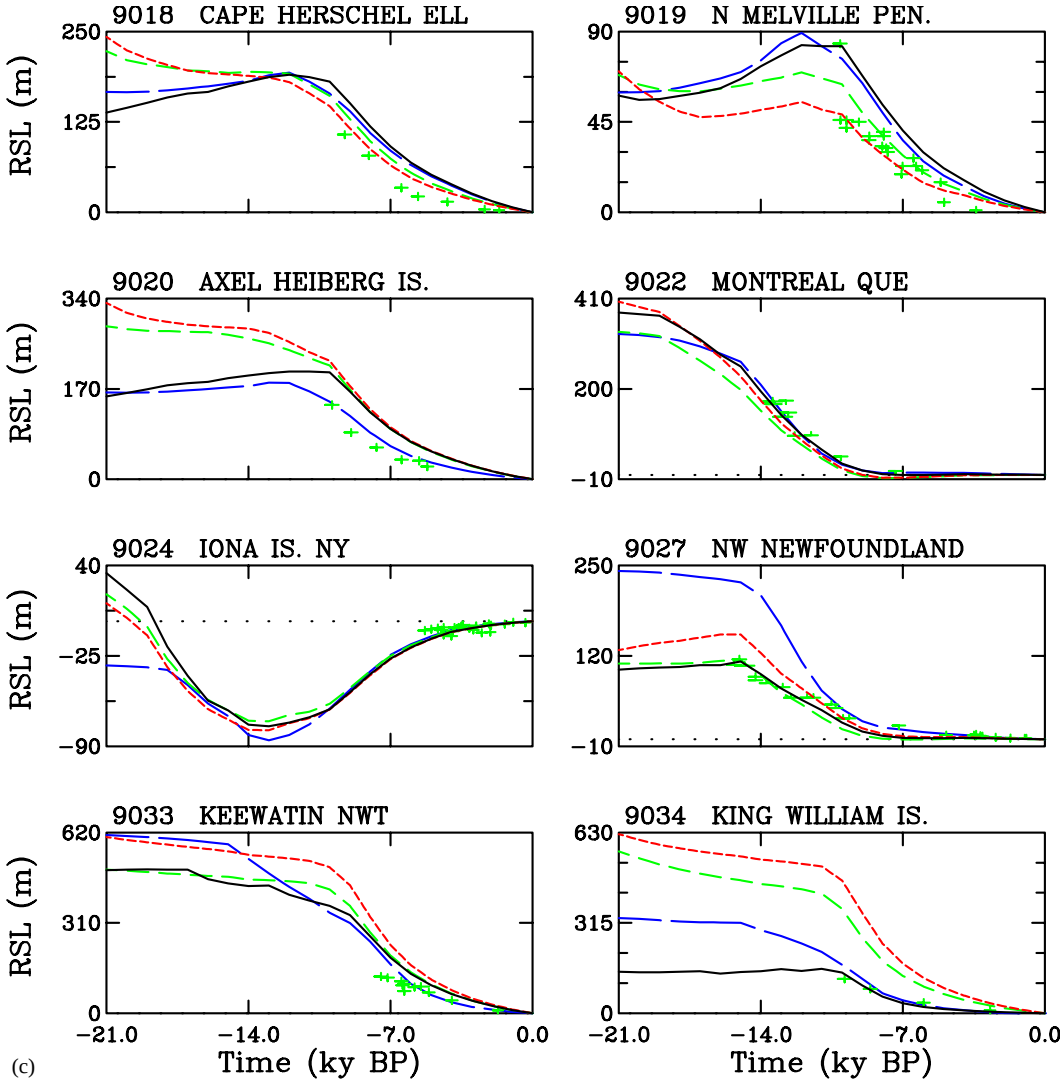

Fig. 10 (*continued*).

ascertain. Without ad hoc mass-balance forcing, our model is unable to obtain the strong drawdown that model nn2059 requires to fit the RSL data. However, a recent analysis employing a different ISM, linear till-deformation law, equilibrium conditions, and much larger glacial ice volume (Calov et al., 2002) has been able to obtain extensive draw-downs over both regions of the order required by model nn2059. Resolution of this issue must await detailed analyses with models that incorporate explicit ice stream physics (i.e. longitudinal and horizontal shear stresses). What is nevertheless clear is that H1/H0 drawdowns from these basins must be very strong in order to have a significant impact on RSL chronologies. A variant of model nn2059 that used somewhat weaker (and arguably more plausible) H1/H0 forcing (1700 and 1300 m ice thickness restrictions over Hudson Bay and no forcing over Foxe Basin) produced clearly inferior fits around Hudson Bay and Foxe Basin (shown in Fig. 2 as model nn2016). Examination of the deglaciation chronology for model nn2059 (Fig. 12) partly explains why such strong H1/H0 forcing is required. There is a tendency for Hudson Bay and Foxe Basin ice to fill in following the strong H0 forcing, thereby negating some of the impact of the forcing on computed RSL histories.

The deglaciation chronology for model nn2059 (Fig. 12) has two other features worth noting. First, as has previously been demonstrated with a much simpler 1D model (Pollard, 1983), inundation of most of the ice marginal perimeter through the appearance of pro-glacial lakes can permit strong calving along much of the ice margin, thereby offering an explanation for the fast rate of deglaciation of the Laurentide Ice Sheet. Details concerning marine heat capacity and ice-berg drainage would, however, require attention before robust conclusions could be drawn in this regard.

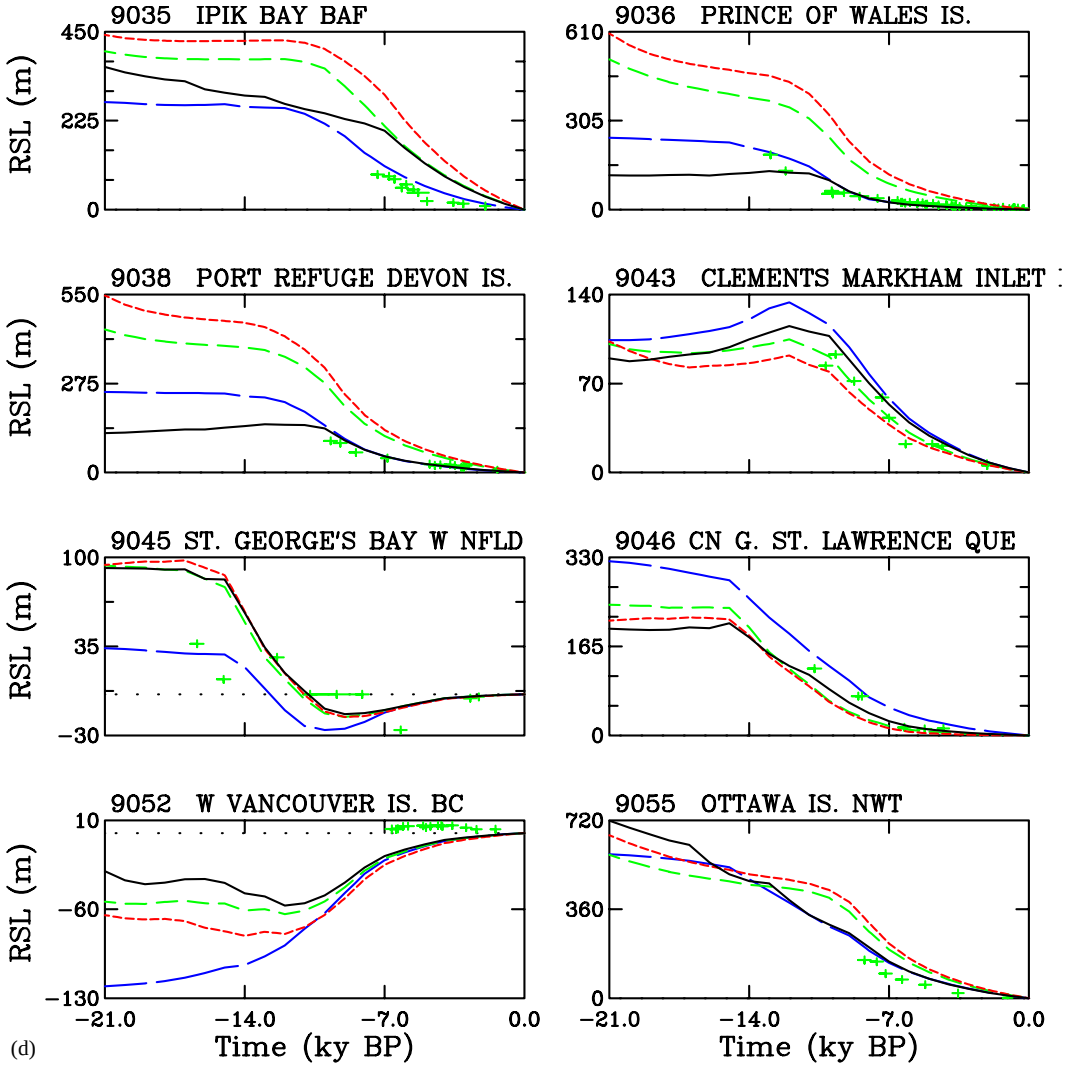

Fig. 10 (*continued*).

Secondly, it is worth noting the persistence of a significant Keewatin dome until approximately −11 kyr. This could have significant impact on atmospheric dynamics over the Laurentide platform and will need attention in future paleo-model intercomparison projects examining Wisconsin deglaciation.

Glaciological analyses of field data have previously inferred a three dome structure for the late glacial Laurentide ice complex (Dyke and Prest, 1987). The dome structure of model nn2059 at LGM lacks both distinct southeast and Foxe Basin domes (Fig. 4), though both of these do occur prior to LGM (not shown). Clearly, articulated domes also emerge by −18 kyr in the southeast and by −16 kyr centered over Baffin island. As well, other models such as nn1164 do exhibit distinct southeast domes at LGM. Most interesting is the deglaciation signature registered in the computed present-day rate of vertical displacement for model nn2059. The displacement field (Fig. 13) has three strong centers of vertical uplift centered over the Keewatin, Quebec, and Foxe basin regions along with a weaker center over the Innuitian/northeastern Greenland region. These uplift signatures in some ways integrate deglacial load histories and their close correspondence to independently inferred late glacial ice topographies further validates the quality of our best-fit model.

3.3. Uncertainties: glacial index chronology, margin chronology, and rheology

As a partial test of the robustness of the ensemble-based analyses, we may examine model sensitivity to uncertainties associated with three constant components of the ensemble, respectively, glacial index chronology during deglaciation, margin forcing chronology, and the rheology of the earth model. We choose to use model nn2016 (which has weaker H1/H0 forcing than our best-fit model 2059) as the base model for our sensitivity

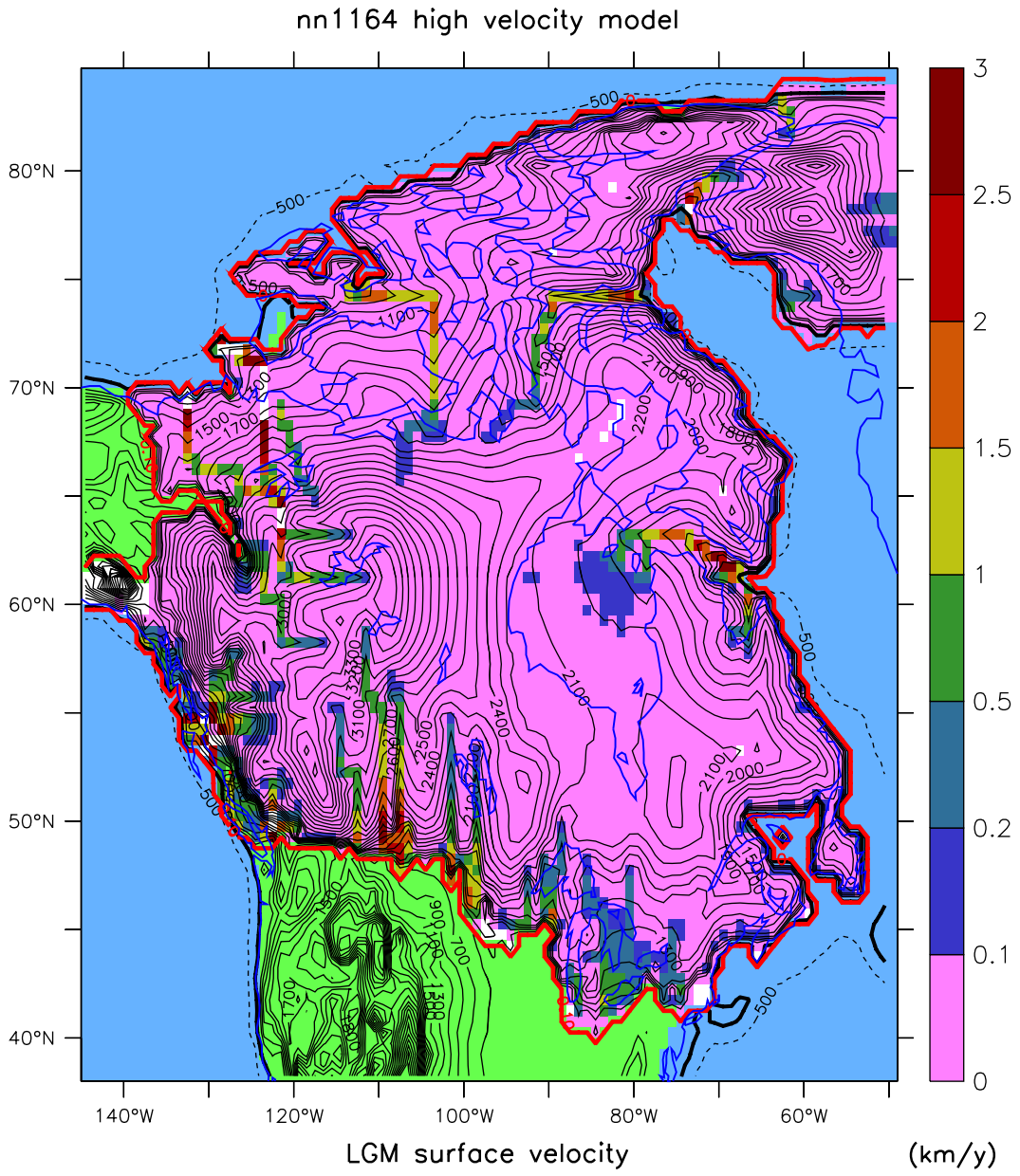

Fig. 11. LGM ice-surface velocity and topography for model nn1164.

analyses so that we can better examine what other mechanisms might allow better fits to the RSL data without the possibly excessive H1/H0 forcing of model 2059.

The use of a downstream paleo record (GRIP $\delta^{18}O$) as a proxy for the time dependence of the climate forcing is a significant limitation of the current analyses. Initial ensemble studies without margin forcing resulted in margin chronologies approximately 3 kyr in advance of the inferred chronology for models tuned to the RSL data. On the other hand, recent analyses with a dynamical ice-sheet model forced by a number of deglacial time slices from a GCM (Charbita et al., 2002) along with earlier analyses using an intermediate complexity climate model (Tarasov and Peltier, 1997) had resultant deglaciation chronologies that were delayed relative to that of the ICE-4G chronology. These diverging results underline the critical importance of margin forcing in our ensemble analyses.

To approximately delineate the role that margin forcing has in reducing the uncertainty associated with climate forcing, we repeated model nn2016 with three different glacial index chronologies during

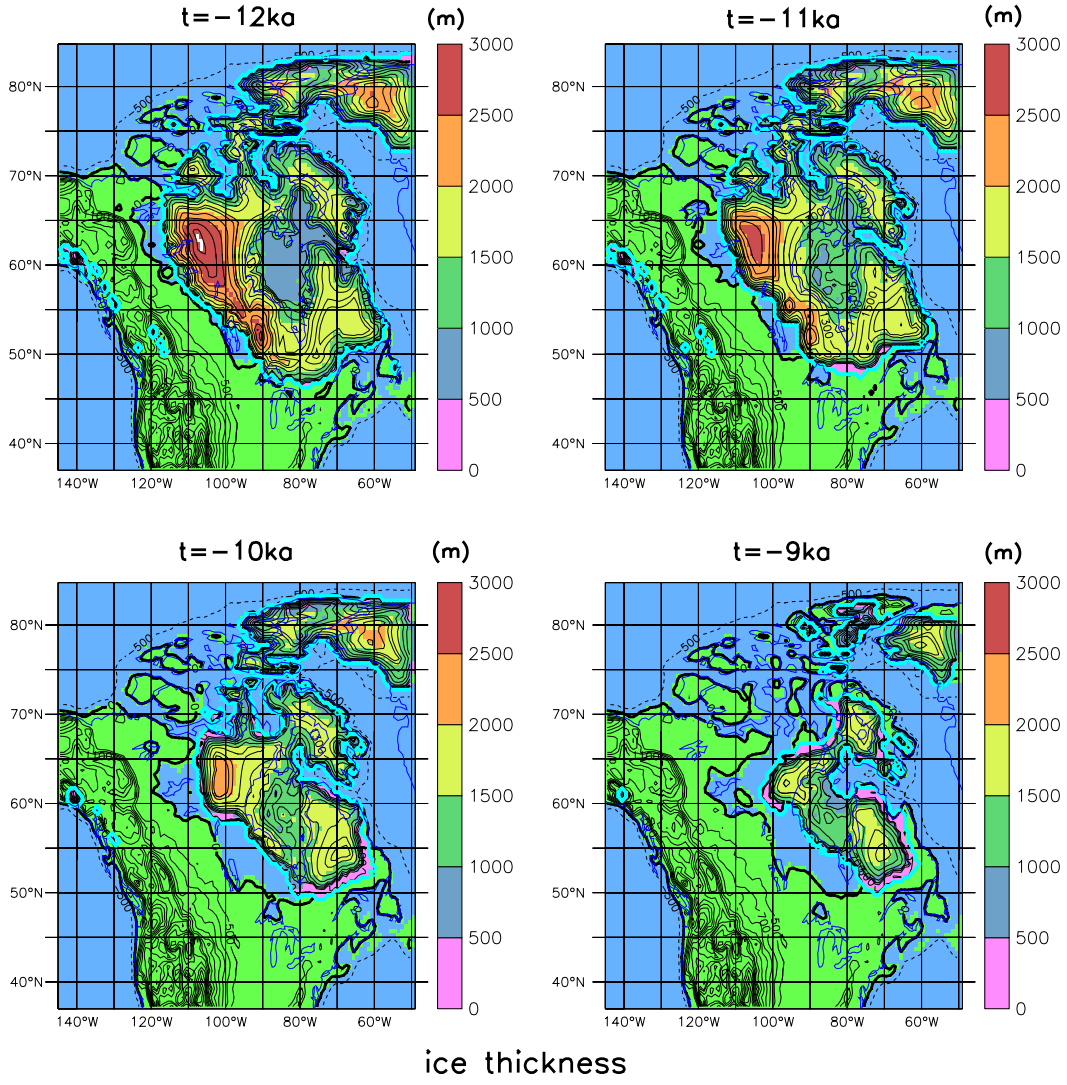

Fig. 12. Deglaciation chronology for model nn2059 using eustatic sea margins.

deglaciation. A warm extremal forcing chronology imposed present-day (i.e. 0 value) glacial index forcing from −21 kyr onward. All other climate forcings (e.g. desert-elevation modifications, etc.) were kept at the corresponding settings for nn2016. For the opposite extreme of climate forcing, we imposed full glacial index forcing (value = 1) from LGM to −8 kyr. As a further test of model sensitivity to a less extreme climate modification, a run was performed in which the glacial index was varied linearly from −20 (value 1) to −10 kyr (value = 0). Through the examination of eight representative sites, it is clear that interior RSL chronologies are largely robust to climate chronology uncertainties (Fig. 14), especially given RSL data point uncertainties and the nature of the climate forcing chronologies imposed. However, more marginal regions, such as the eastern margin of Baffin Island (site 9011) and Axel Hieberg island in the High Arctic (9020), were found to be sensitive to warmer deglacial chronologies but not to colder chronologies.

The relative robustness of the core model RSL chronologies is largely due to the margin forcing imposed on the model. As such, consideration of input margin chronology uncertainty is also warranted. Given that both the RSL and margin chronologies are derived from ^{14}C dated samples, uncertainties in ^{14}C calibration are unlikely to contribute significant error to the RSL fits, even if the rest of the model (and glacial index forcing) is subject to physical calendar year chronologies. As such, the margin chronology uncertainty is estimated to be about ±500 yr (A.S. Dyke, per. comm., 2003), largely due to the temporal resolution of the chronology. We have therefore repeated model 2016 with ±500 shifts in the margin forcing. Not unexpectedly, the impact of the shifts is relatively minor (Fig. 15), though advancement of the margin forcing chronology

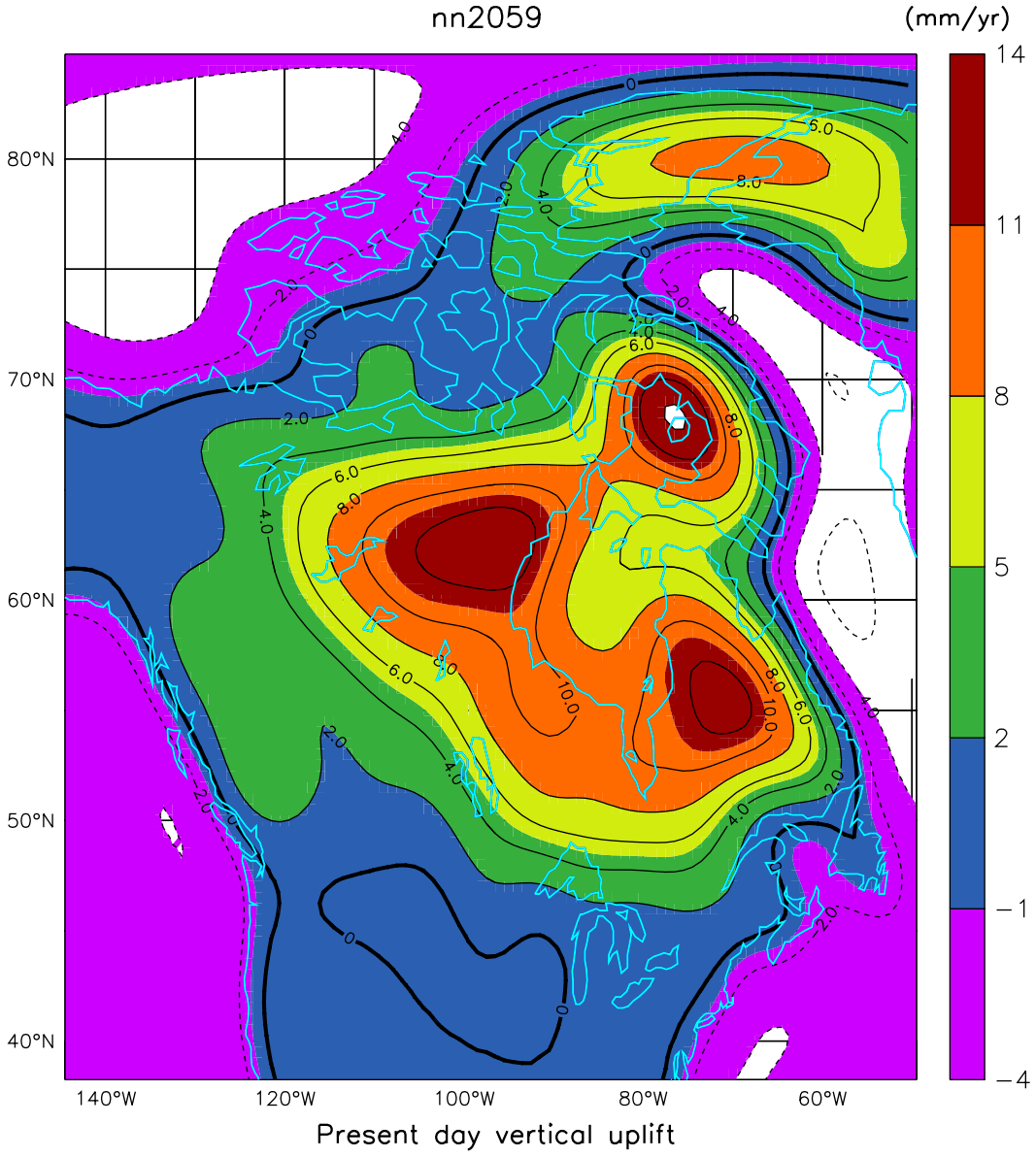

Fig. 13. Present-day rate of uplift for model nn2059.

by 500 yr generally improves RSL fits. This is most significant for the key southeast Hudson Bay site (9003) where an excellent RSL fit is then achieved.

Also shown in Fig. 15 is model nn2016, repeated without H1/H0 forcing. It is evident that this arguably extreme forcing plays a critical role in improving model fits for Hudson Bay region sites. Better constraints on possible H1/H0 drawdowns of Hudson Bay ice would contribute in an important way to further constraining the model.

A remaining uncertainty that has not been fully examined in the glaciological literature is that associated with the assumed viscoelastic structure of the earth model. The need for strong H1/H0 forcing to achieve reasonably good fits in the core Hudson Bay region of the Laurentide Ice Sheet already suggests that the VM2 model utilized is, if anything, an upper bound viscosity model. A much stronger case for this, largely based on a reexamination of Hudson Bay relaxation times, is provided by Dyke and Peltier (2000) and Peltier (2002a). As a lower bound viscosity model, we chose model VM4a which has the viscosity in the VM2 model reduced to 0.9×10^{21} Pa s in the upper part of the lower mantle covering the range of radii from 4904 to 5700 km. Model nn2016 with earth model VM4a produced RSL chronologies that insignificantly differ from those produced with the standard VM2 model (solid line, Fig. 16) for both 90 km (short dashed) and

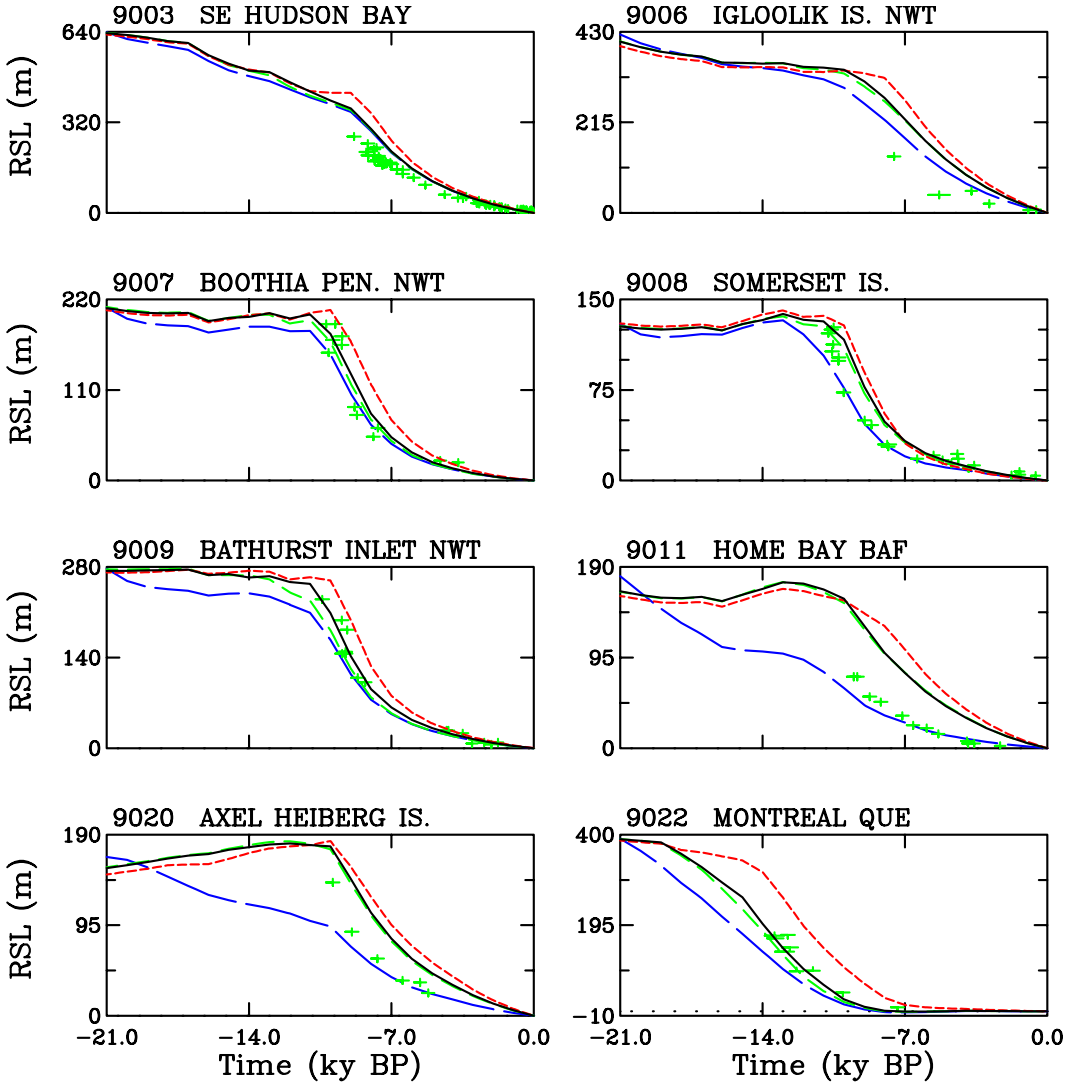

Fig. 14. RSL sensitivity to climate forcing chronology. Deglacial climate chronology was replaced by warm extreme (long dashed blue), linear (medium dashed green), and cold extreme (short dashed red). Base model is nn2016 (solid black line).

120 km lithospheric thicknesses (not shown). It appears that the loading history of model nn2016 does not induce an isostatic adjustment of the surface that departs significantly from that of VM2 in so far as deglacial RSL chronologies are concerned. On the other hand, the larger volume and faster flow model nn1164 (medium and long dashed in Fig. 16, the latter with VM4a and 120 km lithospheric thickness) was significantly more sensitive to the new earth model at certain sites. The use of VM4a significantly improves the fit of model nn1164 to the data from southeast Hudson Bay (site 9003) such that it is now equivalent to the fit provided by model nn2016. However, the imposition of this softer rheology provides no significant help in improving the nn1164 RSL misfits in the Foxe Bay region (Igloolik, site 9006), Baffin Island (Home Bay, 9011), and Lancaster Sound regions (9016–7, 9038).

Taken as a whole, the above sensitivity analyses suggest that RSL-related ensemble results for the core regions of the ice sheet are rather robust to uncertainties associated with the glacial index climate forcing, margin chronology uncertainties, and earth model rheology. Margin forcing uncertainty in combination with earth rheology uncertainty can enable an excellent fit to the RSL data at southeast Hudson Bay for model nn1164 which does not have ad hoc H1/H0 forcing. However, these uncertainties are far short of what is needed to correct model nn1164 RSL misfits in the Lancaster Sound (/Gulf of Boothia) and Foxe Basin regions. As such, the strong H1/H0 forcing introduced in model 2059 for Foxe Basin and its use of strong Arctic calving to produce open-water conditions (or equivalently extensive ice shelves) appears to be difficult to avoid in order to obtain acceptable fits to the RSL data in these regions.

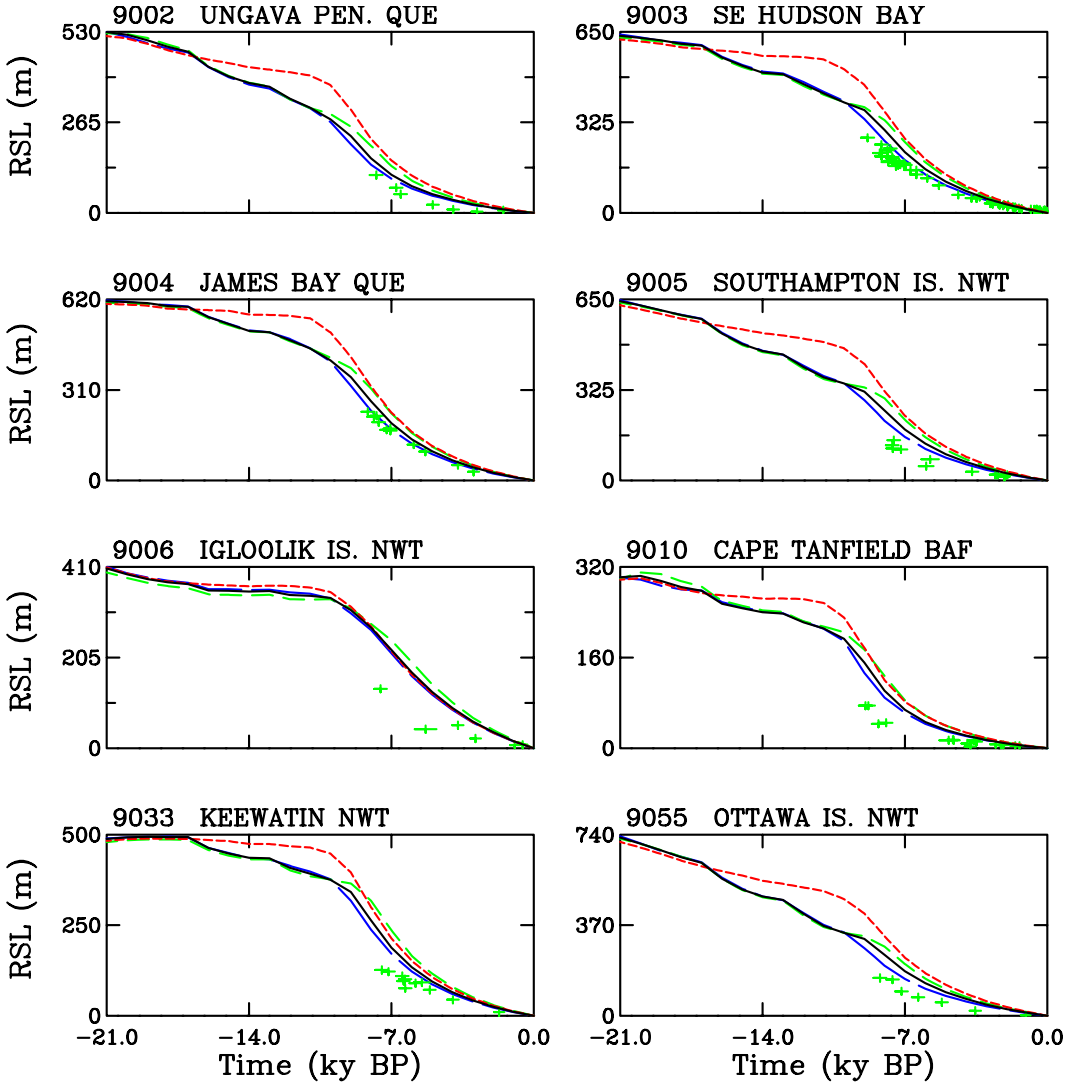

Fig. 15. RSL sensitivity to margin forcing chronology and Heinrich events H1/H0 forcing. Margin forcing was shifted by 500 yr (long dashed blue and medium dashed green), and H1/H0 drawdown forcing was removed (short dashed red) from base model nn2016 (solid black line).

3.4. Ensemble constraints on NA eustatic sea-level contributions

A key issue that has yet to be resolved is the eustatic sea-level contribution from NA that contributed to the approximately 120–130 m LGM drop inferred on the basis of the Barbados and Sunda Shelf records (Fairbanks, 1989; Bard et al., 1990; Hanebuth et al., 2000) as discussed in Peltier (2002b). At −23 kyr (just prior to the imposition of margin forcing), secondary sieved ensemble contributions to the eustatic fall of sea-level range from a lower bound of approximately 50 m to an upper bound of approximately 85 m eustatic (Fig. 17). The lower bound is increased to 59 m if we eliminate runs that had −23 kyr ice area below that covered by the LGM margin data (subject to ±50 km and one grid-box uncertainty), a value that is very close to that of ICE-4G. This area constraint has no impact on the upper bound estimate. The impact of the constraint metric (i.e. secondary sieve) is clearly significant when one considers the much higher 105 m upper bound that obtains when only the primary sieve is employed. Another ensemble-based model study (Marshall et al., 2002) using a much more restricted exploration of the deglaciation phase space (with only 190 runs) and with only LGM area and maximum southern extent constraints (i.e. neither RSL, $\dot{R}$, nor $\dot{g}$ constraints and no margin forcing) obtained a likely LGM eustatic range of 78–88 m for NA. This estimate is non-overlapping with that produced by our secondary sieve analyses (with the additional area bounds imposed), further emphasizing the important role of the RSL and geodetic data in constraining estimates of the eustatic sea-level contributions. Unless much larger H1/H0 drawdown events than that forced

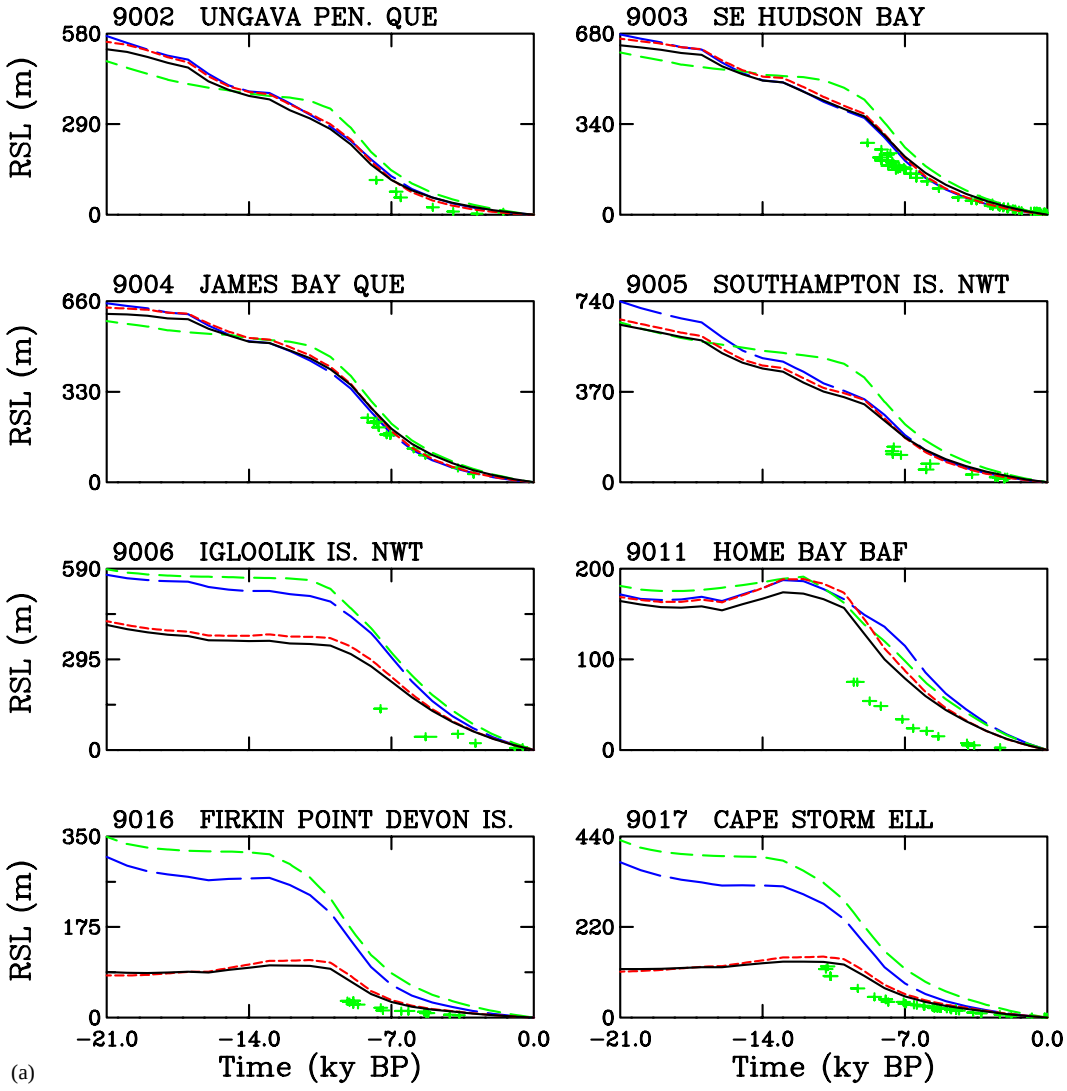

Fig. 16. Impact of Earth model on models nn1164 (medium-dashed green line) and nn2016 (solid black line) RSL for most sensitive sites. VM4a viscosity structure was used with 120 km thick lithosphere on model nn1164 (long dashed blue line) and 90 km thick lithosphere on model nn2016 (short dashed red line): (a) and (b).

in model nn2059 are allowed (or if possibly some hitherto unexplained mechanism for significantly reducing Hudson Bay and Foxe Basin basal surface loads during mwp1a that is consistent with the paleo-oceanographic record could be found, contrary to Clark et al., 1996a), large mass models of the kind described in Marshall et al. (2002) are unable to fit the RSL constraints when subject to the margin chronology constrained deglaciation history.

One further issue is whether a significant reduction in ice volume from −23 to −20 kyr is physical. For most of the larger LGM ice volume runs that passed the two sieves, reductions equivalent to order 10 m eustatic sea-level change occur, largely as a result of the ice dynamical response to the initiation of margin forcing. As such, one could argue that runs with a significant reduction had excessive pre-LGM ice, and should therefore be eliminated. By imposing this condition, a primary sieved upper bound is reduced to about 80 m, while a secondary sieved upper bound would be near 70 m at −20 kyr (Fig. 17).

The inclusion of the requirement for glaciological self-consistency along with the new $\dot{R}$ and $\dot{g}$ constraints has a significant impact on the inferred NA eustatic sea-level chronology. In Fig. 18 are shown eustatic sea-level chronologies for two base models along with extremal members from the secondary sieved ensemble subject to the above-mentioned area constraints. It should be noted that the two larger volume models (nn1098 and nn1164) have excessive inception sea-level peaks at −106.5 kyr due to the extra (+0.2) glacial index forcing that is applied during

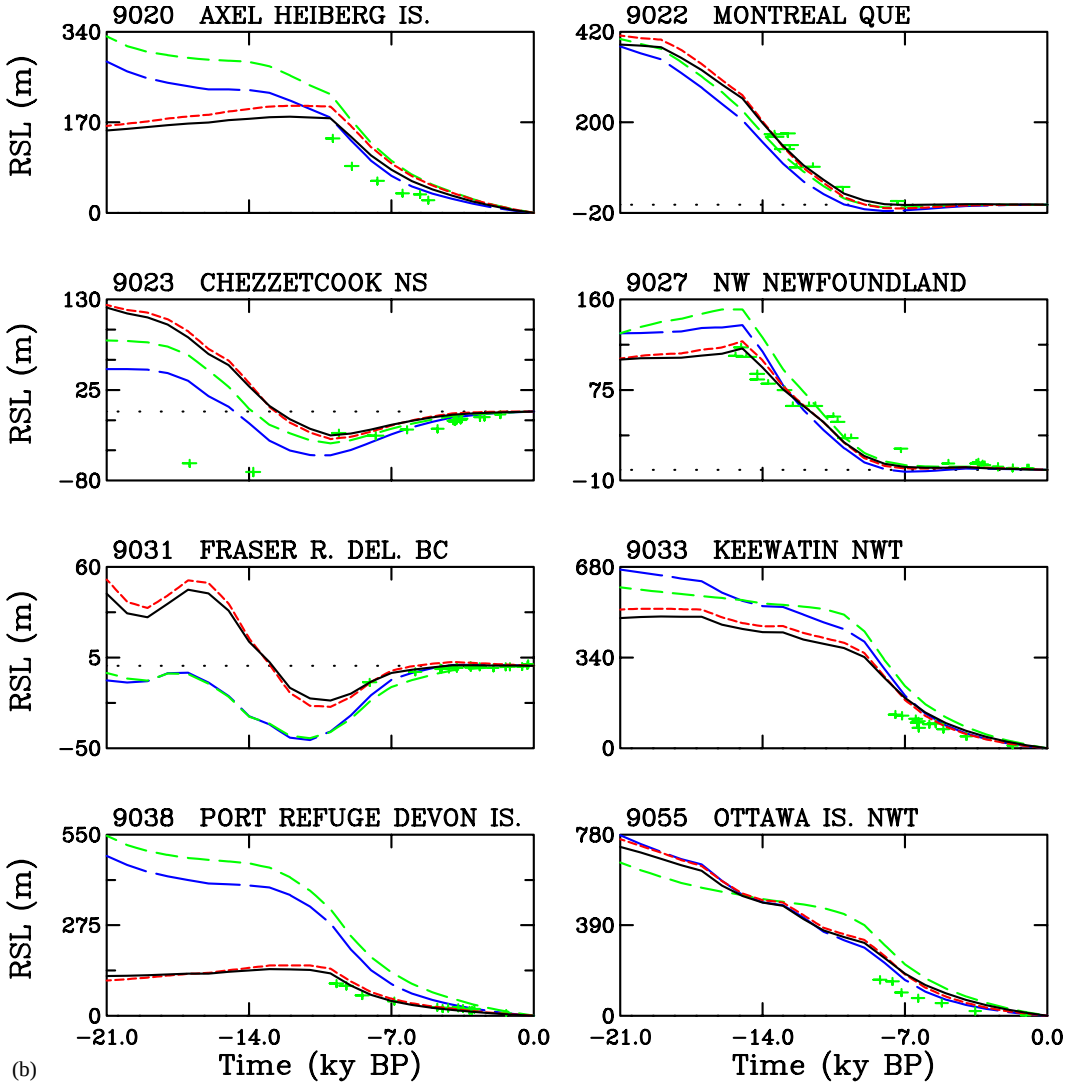

(b)

Fig. 16 (*continued*).

the inception period (as described in the previous subsection on climate forcing). It therefore appears that this ad hoc adjustment of the inception forcing is not required for all of the models. Since our analyses are focused on the deglaciation period, this excessive inception period ice growth is largely irrelevant to the discussions herein.

All these models have much more ice volume than ICE-4G during the whole LGM and deglacial period. Furthermore mwp1a (terminating at −14 kyr) is significantly reduced to about 10 m eustatic for the glaciological models in comparison to the 18 or more meter contribution of ICE-4G. This is in better agreement with paleo-oceanographic inferences on the size of the NA contribution to mwp1a (Clark et al., 1996a). The reduction in the contribution to mwp1a from the glaciological models appears to account for much of the difficulty in obtaining good fits to Hudson Bay region RSL observations. As described earlier, model nn2059 incorporates H1/H0 (Heinrich event forced reductions in Hudson Bay and Foxe Basin ice thickness) to improve the core region fits. The impact of this H1/H0 forcing is also evident with the resultant order 5 m eustatic sea-level drops for model nn2059 relative to other glaciological models. In future work, we will examine in detail the extent to which the amplitude of mwp1a is actually constrained by models of the kind that we have developed.

4. Conclusions

Our ensemble-based analyses provide a number of significant constraints on the deglacial evolution of the North American (NA) ice-sheet complex. Firstly, the

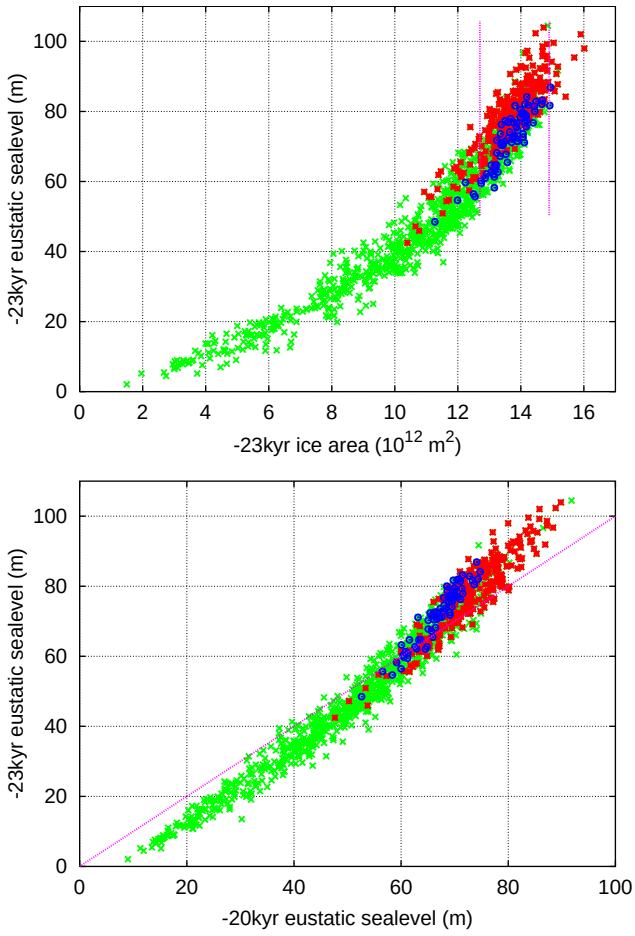

Fig. 17. Ensemble results for LGM eustatic sea level contribution from NA. Bounds for ice area (obtained from input margin chronology, refer to text) are shown in upper plot.

NA contribution to Last Glacial Maximum (LGM) eustatic sea-level change is likely to lie in the range of 60–75 m (Fig. 18). This increase in sea-level contribution relative to that of ICE-4G will clearly play an important role in accounting for the approximately 130 m global eustatic LGM sea-level drop that the Sunda Shelf data suggests to have occurred (Peltier, 2002b).

Secondly, Hudson Bay relative sea-level (RSL) observations (and $\dot{g}$ transect data) appear to require a thin core region and/or major drawdowns of Hudson Bay ice during deglaciation. As an explanation of this thin core, we hypothesize that significant atmospheric reorganization due to the presence of a large Keewatin dome resulted in moisture starvation over the Hudson Bay region. GCM modelling of LGM climate with a large Keewatin dome will provide a test of this hypothesis.

Thirdly, RSL observations for the north-central region (Lancaster Sound to the Gulf of Boothia) appear to require an extended ice shelf and/or open water from LGM or earlier. The Eclipse Moraines (on the south shore of Lancaster Sound) indicate that thick grounded ice was present during part of the glacial period, possibly at LGM, though the moraines are not well-dated (A.S. Dyke, per. comm., 2003). It is likely that once the regional ice was fully grounded, grounding-line recession would have had to await either extensive moisture starvation and/or significant sea-level rise. As such, reconciliation of the existence of these moraines with our model analyses remains a challenge.

Fourthly, our analyses have demonstrated the critical role that geographically constrained fast flows due to till deformation have in creating a multi-domed Laurentide Ice Sheet. We are not able to obtain such well-defined topographic structures with only strong sliding. RSL constraints in turn favor ensemble models with relatively thin ice in the central and northern regions. Given the inferred margin extent this can only be obtained by fast flows and/or deep calving.

Finally, results of direct geophysical observations have also been shown to place strong constraints on model ice-sheet evolution as previously demonstrated in Peltier (2002a). VLBI uplift data from Yellowknife requires a Keewatin ice dome with peak thickness between approximately 3.3 and 4.3 km. The transect of $\dot{g}$ observations also requires a thick ice ridge south of Hudson Bay. The thick ice ridge in combination with southern Hudson Bay and James Bay RSL data also further limits the possible late glacial thickness of Hudson Bay ice.

The outstanding issue that remains is the validity of the strong H1/H0 ice drawdowns that the model appears to require for the Foxe Basin region and possibly for the Hudson Bay region (the latter subject to earth rheology and margin timing uncertainties). The dynamical viability of such large drawdowns will need to be examined in detail. Temporal controls on fast flow due to basal hydrology are also likely to play an important role but are a challenge to accurately constrain. It is also unlikely that such drawdowns could be transferred to the melt-water pulse 1a event given the paleo-oceanographic record, although this remains to be considered in greater detail. Further constraints upon the deglaciation of the NA ice-sheet complex will also benefit from more data for regions with limited data coverage such as Western Canada and central/northern Quebec and Labrador.

Our best-fit hand-tuned model (nn2059) provides good fits to the RSL data for most regions aside from Baffin Island and the northwest Arctic. $\dot{g}$ transect values also indicate that the model lacks sufficient south-central near-marginal ice. It is a testament to the quality of past glaciological interpretations that our best fit models have LGM surface topographies close to that

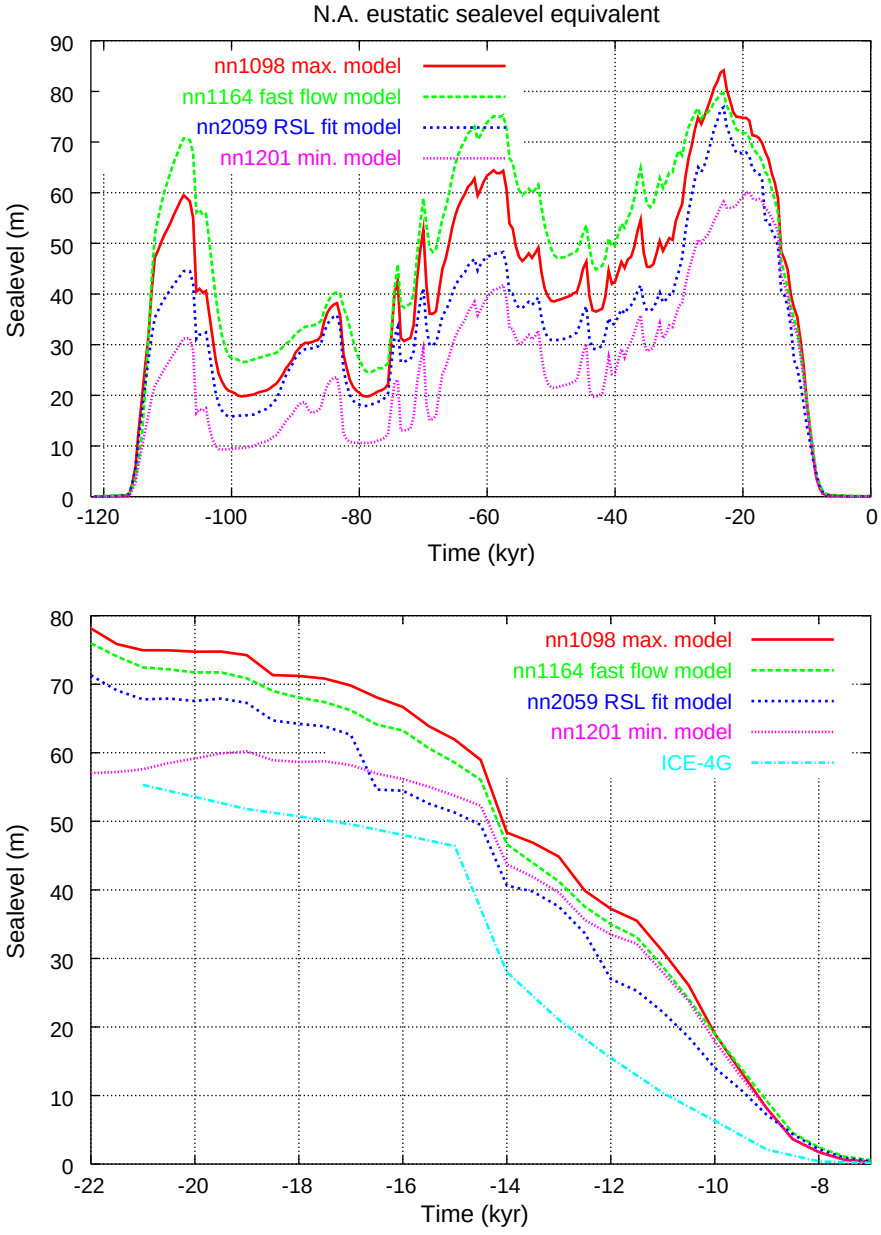

Fig. 18. Eustatic sea-level contributions from best-fit, secondary and LGM area sieved boundaries, and ICE-4G models.

predicted a decade and a half ago (Dyke and Prest, 1987). Though significant evolution of this model is ongoing, our results already indicate that geophysical observations are largely reconcilable with current state-of-the-art-coupled ISMs once proper allowance is made for model input uncertainties. In a next step in this series of analyses of the physical processes that control Laurentide Ice Sheet form and evolution, a further revised methodology based upon the Bayesian calibration of a neural network emulator of the glacial cycle model along with the incorporation of explicit ice-stream and ice-shelf physics, should provide clear error bars and further improved fits to the observations.

Acknowledgements

This paper is a contribution to the Climate System History and Dynamics Collaborative Research Network that is funded by the Natural Sciences and Engineering Research Council of Canada and the Atmospheric Environment Service of Canada. Additional support for the work has been provided by NSERC Grant A9627. This work has benefited from extensive discussions with Art Dyke of the Geological Survey of Canada. This work has also benefited from an on-going collaboration with Radford Neal at the University of Toronto in the development of a Bayesian calibration of the deglaciation model.

References

Alley, R.B., 1991. Deforming-bed origin for southern Laurentide till-sheets? Journal of Glaciology 37 (125), 67–76.

Andrews, J.T., MacLean, B., 2003. Hudson Strait ice streams: a review of stratigraphy, chronology and links with North Atlantic Heinrich events. Boreas 32 (1), 4–17.

Argus, D.F., Peltier, W.R., Watkins, M.M., 1999. Glacial isostatic adjustment observed using very long baseline interferometry and satellite laser aging geodesy. Journal of Geophysical Research 104, 29077–29093.

Bard, E., Hamelin, B., Fairbanks, R.G., Zindler, A., 1990. Calibration of the ^{14}C timescale over the past 30,000 years using mass spectrometric U/Th ages from Barbados corals. Nature 345, 405–409.

Bishop, C.M., 1995. Neural Networks for Pattern Recognition. Clarendon Press, Oxford.

Braithwaite, R.J., 1995. Positive degree-day factors for ablation on the Greenland ice sheet studied by energy-balance modeling. Journal of Glaciology 41 (137), 153–160.

Budd, W.F., Smith, I.N., 1981. The growth and retreat of ice sheets in response to orbital radiation changes. In: Sea Level, Ice and Climatic Changes. Vol. 131. IAHS, pp. 369–409, Canberra, Australia.

Calov, R., Ganopolski, A., Petoukhov, V., Claussen, M., Greve, R., 2002. Large-scale instabilities of the Laurentide ice sheet simulated in a fully coupled climate-system model. Geophysical Research Letters 29 (24), 2216.

Charbita, S., Ritz, C., Ramstein, G., 2002. Simulations of Northern Hemisphere ice-sheet retreat: sensitivity to physical mechanisms involved during the Last Deglaciation. Quaterly Science Review 21, 243–265.

Clark, P., Alley, R., Keigwin, L., Licciardi, J., Johnsen, S., Wang, H., 1996a. Origin of the first global meltwater pulse following the Last Glacial Maximum. Paleoecologia 11 (5), 563–577.

Clark, P.U., MacAyeal, J.M.L.D.R., Jenson, J.W., 1996b. Numerical reconstruction of a soft-bedded Laurentide ice sheet during the Last Glacial Maximum. Geology 24 (8), 679–682.

Deblonde, G., Peltier, W.R., Hyde, W.T., 1992. Simulations of continental ice sheet growth over the last glacial–interglacial cycle: experiments with a one level seasonal energy balance model including seasonal ice albedo feedback. Global and Planetary Change 98, 37–55.

Dyke, A.S., 2003. An outline of North American deglaciation with emphasis on central and northern Canada. In: Ehlers, J. (Ed.), Extent and Chronology of Quaternary Glaciation. Elsevier.

Dyke, A.S., Peltier, W.R., 2000. Forms, response times and variability of relative sea level curves, glaciated North America. Geomorphology 32, 315–333.

Dyke, A.S., Prest, V.K., 1987. Late Wisconsinan and Holocene history of the Laurentide ice sheet. Geographie Physique et Quaternaire 41, 237–264.

Dyke, A.S., Andrews, J.T., Clark, P.U., England, J.H., Miller, G.H., Shaw, J., Veillette, J., 2002. The Laurentide and Innuitian ice sheets during the Last Glacial Maximum. Quaternary Science Reviews 21, 9–31.

Dyke, A.S., Moore, A., Robertson, L., 2003. Deglaciation of North America. Technical Report Open File 1574, Geological Survey of Canada, thirty-two maps at 1:7,000,000 scale with accompanying digital chronological database and one poster (in two sheets) with full map series.

Fairbanks, R.G., 1989. A 17,000-year glacio-eustatic sea level record: influence of glacial melting rates on the Younger Dryas event and deep-ocean circulation. Nature 342, 637–641.

Goodman, P.H., Harrel, F.E., 1999. Neural networks: advantages and limitations for statistical modeling. In: Proceedings of the Biometrics Section, Joint Statistical Meeting, American Statistical Association, Alexandria, VA.

Hamilton, T.D., 1994. The Geology of Alaska, In: Plafker, G., Berg, H.C. (Eds.), Vol. G1. Geological Society of America, Boulder, CO. pp. 145–172 (Chapter on Late Cenozoic Glaciation of Alaska).

Hanebuth, T., Stattegger, K., Grootes, P.M., 2000. Rapid flooding of the Sunda Shelf: a late glacial sea level record. Science 288, 1033–1035.

Imbrie, J., J.D.H., Martinson, D., McIntyre, A., Mix, A.C., Morley, J.J., Pisias, N.G., Prell, W.L., Shackleton, N.J., 1984. Milankovitch and Climate. In: Reidel, D. (Ed.), The Orbital Theory of Pleistocene Climate: Support from a Revised Chronology of the Marine $\delta^{18}O$ Record, pp. 269–305.

Janssens, I., Huybrechts, P., 2000. The treatment of meltwater retention in mass-balance parameterizations of the Greenland ice sheet. Annals of Glaciology 31, 133–140.

Jenson, J.W., MacAyeal, D.R., Clark, P.U., Ho, C.L., Vela, J.C., 1996. Numerical modeling of subglacial sediment deformation: implications for the behaviour of the Lake Michigan Lobe, Laurentide Ice Sheet. Journal of Geophysical Research 101 (B4), 8717–8728.

Johnsen, S.J., Dansgaard, W., White, J.W.C., 1989. The origin of Arctic precipitation under present and glacial conditions. Tellus 41, 452–469.

Kalnay, E. et al., 1996. The NCEP/NCAR 40-year reanalysis project. Bulletin of the American Meteorological Society 77, 437–471.

Kleman, J., Hattestrand, C., 1999. Frozen-bed Fennoscandian and Laurentide ice sheets during the Last Glacial Maximum. Nature 402 (6757), 63–66.

Lambert, A., Courtier, N., Sasegawa, G.S., Klopping, F., Winester, D., James, T., Liard, J.O., 2001. New constraints on Laurentide postglacial rebound from absolute gravity measurements. Geophysical Research Letters 28, 2109–2112.

Laske, G., Masters, G., 1997. A global digital map of sediment thickness. EOS Trans. 78, F483.

Legates, D.R., Willmott, C.J., 1990. Mean seasonal and spatial variability in gauge-corrected global precipitation. International Journal of Climatology 10 (2), 111–127.

Licciardi, J.M., Clark, P.U., Jenson, J.W., Macayeal, D.R., 1998. Deglaciation of a soft-bedded Laurentide Ice Sheet. Quaternary Science Reviews 17 (4–5), 427–448.

MacAyeal, D.R., 1993. Binge/purge oscillations of the Laurentide ice sheet as a cause of the North Atlantic's Heinrich events. Paleoceanology 8, 775–784.

Marshall, S.J., 2002. Modelled nucleation centres of the Pleistocene ice sheets from an ice sheet model with subgrid topographic and glaciologic parameterizations. Quaternary International 95–96, 125–137.

Marshall, S.J., Tarasov, L., Clarke, G.K.C., Peltier, W.R., 2000. Glaciology of Ice Age cycles: physical processes and modelling challenges. Canada Journal of Earth Science 37, 769–793.

Marshall, S.J., James, T.S., Clarke, G.K.C., 2002. North American Ice Sheet reconstructions at the Last Glacial Maximum. Quaternary Science Reviews 21, 175–192.

Paterson, W.S.B., 1994. The Physics of Glaciers. Pergamon, Tarrytown N.Y.

Payne, A.J., Dongelmans, P.W., 1997. Self-organization in the thermomechanical flow of ice sheets. Journal of Geophysical Research 102 (B6), 12219–12234.

Payne, A.J.., et al., 2000. Results from the EISMINT model intercomparison: the effects of thermomechanical coupling. Journal of Glaciology 46 (153), 227–238.

Peltier, W.R., 1974. The impulse response of a Maxwell Earth. Review of Geophysics 12, 649–669.

Peltier, W.R., 1976. Glacial isostatic adjustment II: the inverse problem. Geophysical Journal of the Royal Astronomical Society 46, 669–706.

Peltier, W.R., 1994. Ice age paleotopography. Science 265, 195–201.
Peltier, W.R., 1996. Mantle viscosity and ice age ice sheet topography. Science 273, 1359–1364.
Peltier, W.R., 1998a. "Implicit ice" in the global theory of glacial isostatic adjustment. Geophysical Research Letters 25 (21), 3955–3958.
Peltier, W.R., 1998b. Postglacial variations in the level of the sea: implications for climate dynamics and solid-earth geophysics. Review of Geophysics 36, 603–689.
Peltier, W.R., 2002a. Global glacial isostatic adjustment: paleo-geodetic and space-geodetic tests of the ICE-4G (VM2) model. Journal of Quaternary Science 17 (5–6), 491–510.
Peltier, W.R., 2002b. On eustatic sea level history, Last Glacial Maximum to Holocene. Quaternary Science Reviews 21, 377–396.
Peltier, W.R., 2003. On the hemispheric origins of meltwater pulse 1a. Quaternary Science Reviews, submitted.
Peltier, W.R., Jiang, X., 1996. Mantle viscosity from the simultaneous inversion of multiple data sets pertaining to postglacial rebound. Geophysical Research Letters 23, 503–506.
Piotrowski, J.A., Mickelson, D.M., Tulaczyk, S., Krzyszkowski, D., Junge, F.W., 2002. Reply to the comments by G.S. Boulton, K.E. Dobbie, S. Zatsepin on: Deforming soft beds under ice sheets: how extensive were they? Quaternary International 97–98, 173–177.
Pollack, H.N., Hurter, S.J., Johnson, J.R., 1993. Heat flow from the Earth's interior: analysis of the global data set. Review of Geophysics 31, 267–280.
Pollard, D., 1983. Ice-age simulations with a calving ice-sheet model. Quaternary Research 20, 30–48.
Pollard, D. PMIP-participating groups, 2000. Comparisons of ice-sheet surface mass budgets from paleoclimate modeling intercomparison project (pmip) simulations. Global and Planetary Change 24, 79–106.
Stokes, C.R., Clark, C.D., 2001. Palaeo-ice streams. Quaternary Science Reviews 20, 1437–1457.
Stuiver, M., Reimer, P.J., Bard, E., Beck, W., Burr, G.S., Hugen, K.A., Kromer, B., McCormac, G., van der Plicht, J., Spurk, M., 1998. INTCAL98 radiocarbon age calibration, 24,000-0 cal BP. Radiocarbon 40, 1041–1084.
Tarasov, L., Peltier, W.R., 1997. Terminating the 100 kyr ice age cycle. Journal of Geophysical Research 102 (D18), 21665–21693.
Tarasov, L., Peltier, W.R., 1999. Impact of thermomechanical ice sheet coupling on a model of the 100 kyr ice age cycle. Journal of Geophysical Research 104, 9517–9545.
Tarasov, L., Peltier, W.R., 2002. Greenland glacial history and local geodynamic consequences. Geophysical Journal International 150, 198–229.
Tarasov, L., Peltier, W.R., 2003. Greenland glacial history, borehole constraints and Eemian extent. Journal of Geophysical Research 108 (B3), 2124–2143.
Van der Veen, C.J., 2002. Calving glaciers. Progress in Physical Geography 26 (1), 96–122.
Vieli, A., Funk, M., Blatter, H., 2001. Flow dynamics of tidewater glaciers: a numerical modelling approach. Journal of Glaciology 47 (595–606).